ADVANCED ELECTRONIC MATERIALS
Open Access
www.advelectronicmat.de

Check for updates

Correlation between Electronic Structure, Microstructure, and Switching Mode in Valence Change Mechanism Al_2O_3/TiO_x-Based Memristive Devices

*Stephan Aussen, Felix Cüppers, Carsten Funck, Janghyun Jo, Stephan Werner, Christoph Pratsch, Stephan Menzel, Regina Dittmann, Rafal Dunin-Borkowski, Rainer Waser, and Susanne Hoffmann-Eifert**

Memristive devices with valence change mechanism (VCM) show promise for neuromorphic data processing, although emulation of synaptic behavior with analog weight updates remains a challenge. Standard filamentary and area-dependent resistive switching exhibit characteristic differences in the transition from the high to low resistance state, which is either abrupt with inherently high variability or gradual and allows quasi-analog operation. In this study, the two switching modes are clearly correlated to differences in the microstructure and electronic structure for $Pt/Al_2O_3/TiO_x/Cr/Pt$ devices made from amorphous layers of 1.2 nm Al_2O_3 and 7 nm TiO_x by atomic layer deposition. For the filamentary mode, operando spectromicroscopy experiments identify a localized region of ≈50 nm in diameter of reduced titania surrounded by crystalline rutile-like TiO_2, highlighting the importance of Joule heating for this mode. In contrast, both oxide layers remain in their amorphous state for the interfacial mode, which proves that device temperature during switching stays below 670 K, which is the TiO_2 crystallization temperature. The analysis of the electronic conduction behavior confirms that the interfacial switching occurs by modulating the effective tunnel barrier width due to accumulation and depletion of oxygen vacancies at the Al_2O_3/TiO_x interface. The results are transferable to other bilayer stacks.

1. Introduction

Redox-based resistive random-access memory (ReRAM) devices with bipolar switching behavior fabricated from material stacks compatible to complementary metal oxide semiconductor (CMOS) technology hold promise for new computational concepts.[1–3] Standard filamentary VCM cells require an electroforming step prior to the subsequent bipolar resistive switching which is based on a temperature-accelerated drift and diffusion of oxygen vacancies leading to the closing and rupture of the conductive filament.[4] Typically, the filament closing representing the SET process comes with an abrupt change from the high (HRS) to low resistance state (LRS). This is due to a configurational change of the switching material in the region between filament tip and active electrode. Several studies address the microstructure of the conductive

S. Aussen, F. Cüppers, C. Funck, S. Menzel, R. Dittmann, R. Waser, S. Hoffmann-Eifert
Peter Grünberg Institut (PGI 7 and 10) and JARA-FIT
Forschungszentrum Jülich GmbH
Wilhelm-Johnen-Straße, 52428 Jülich, Germany
E-mail: su.hoffmann@fz-juelich.de

S. Aussen
RWTH Aachen University
Templergraben 55, 52062 Aachen, Germany

J. Jo, R. Dunin-Borkowski
Ernst Ruska-Center (ER-C-1 / PGI-5) and JARA-FIT
Forschungszentrum Jülich GmbH
Wilhelm-Johnen-Straße, 52428 Jülich, Germany

S. Werner, C. Pratsch
Department X-ray Microscopy
Helmholtz-Zentrum für Materialien und Energie GmbH
Albert-Einstein-Str. 15, 12489 Berlin, Germany

R. Waser
Institute of Materials in Electrical Engineering and Information Technology II
RWTH Aachen University
Sommerfeldstraße 24, 52074 Aachen, Germany

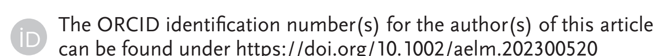
The ORCID identification number(s) for the author(s) of this article can be found under https://doi.org/10.1002/aelm.202300520

© 2023 The Authors. Advanced Electronic Materials published by Wiley-VCH GmbH. This is an open access article under the terms of the Creative Commons Attribution License, which permits use, distribution and reproduction in any medium, provided the original work is properly cited.

DOI: 10.1002/aelm.202300520

2199160x, 2023, 12, Downloaded from https://onlinelibrary.wiley.com/doi/10.1002/aelm.202300520, Wiley Online Library on [11/12/2023]. See the Terms and Conditions (https://onlinelibrary.wiley.com/terms-and-conditions) on Wiley Online Library for rules of use; OA articles are governed by the applicable Creative Commons License

filament in ReRAM cells from single layer TiO_2. From these, Magnéli-type Ti_4O_7 has been identified in the local filament area,[5–7] and also crystalline rutile- and orthorhombic-like TiO_2 phases have been found in the region adjacent to the main reduced filament area.[8] In addition, TiO_x has been shown to be ideal for spectroscopic investigation and therefore has been studied extensively with respect to the filamentary switching mode.[9] The observed changes in the microstructure and -chemistry are consistent with the fundamental understanding of the standard filamentary VCM-type switching process in transition metal oxide-based devices.[10]

In contrast, non-filamentary switching often does not require previous electroforming, and HRS and LRS values scale with the device area. These area-dependent switching devices have attracted attention because they show gradual SET events which allow a quasi-analog programming of the resistance states on time scales from microseconds to seconds. Consequently, this kind of devices has emerged as promising technology for implementing neuromorphic computing like emulation of synaptic behavior in neural networks.[11] The switching mechanism can be either of electronic origin like filling and emptying of traps[12,13] or by exchange of oxygen ions at an interface.[14–16] Both mechanisms give a spatially uniform contribution to the total current leading to an area-dependent switching hysteresis often characterized by low device-to-device and low cycle-to-cycle variation. Interfacial switching has been reported for different perovskite materials, such as $SrTiO_3$[17] and (Pr,Ca)MnO_3[18] but also for oxygen-deficient transition metal oxides like TaO_x,[19–22] NbO_x,[23,24] WO_x,[25,26] HfO_x,[27,28] and TiO_x[29,30] in combination with different tunneling barriers, mostly Al_2O_3. Some material stacks enable operation in either abrupt filamentary or gradual area-dependent switching mode controlled by the operation conditions.

This work focuses on a comprehensive physical understanding of the two bipolar resistive switching modes observed in the same material stack. This is Pt/1.2 nm Al_2O_3/7 nm TiO_x/Cr/Pt (from bottom to top) fabricated on Si/SiO_2 substrates and on Si_3N_4 membrane substrates in the form of micro- and nano-crossbar devices. The metal oxide layers were grown by atomic layer deposition (ALD) at 250 °C and exhibit an amorphous structure for devices in the pristine state. The Al_2O_3/TiO_x bilayer is sandwiched between the high work function Pt electrode and the Cr electrode with higher oxygen affinity, which is protected against continuous oxidation in atmosphere by platinum. The Pt capping layer is given for completeness, however, the active memristor stack is Pt / oxide double layer / Cr. One mode is standard VCM-type filamentary switching which is obtained after an initial electroforming step and characterized by an abrupt SET event occurring at negative voltage applied to the high work function Pt electrode. The filamentary (*f*-) mode serves as a reference for the SET kinetics and for the spectroscopy studies. The second mode is obtained without an electroforming step and reveals a gradual SET event if a voltage signal of positive polarity is applied to the Pt electrode. According to the area-dependence of the programmed resistance states this behavior is named area (*a*-) switching mode.[31] Analyzing the switching characteristics of neighboring devices on the same sample allowed a direct comparison of the two switching characteristics including scalability and SET kinetics with respect to voltage and power. Operando X-ray transmission spectromicroscopy was used to detect local structural and chemical changes showing distinct differences for devices which were switched in the *f*– and *a*–mode. In addition, the extended *I–V* characteristics of the gradual programmed resistive states are compared with a conduction model for electronic transport through the device stack. The numerical calculation reveals that changes in the oxygen vacancy concentration by a factor of about two can cause a modulation of the effective tunnel barrier which is sufficient to explain the observed resistance change between *a*-HRS and *a*-LRS. The results can be applied to various redox-based memristive device stacks consisting of a thin layer of tunnel oxide in combination with a slightly thicker conductive metal oxide layer enriched with defects, thus providing guidance for proper design of area switching devices.

2. Results and Discussion

2.1. Electrical Characterization

2.1.1. Continuous Voltage Sweeps

Representative current-voltage (*I–V*) characteristics for Pt/1.2 nm Al_2O_3/7 nm TiO_x/Cr/Pt devices obtained from continuous voltage sweeps in the range of ± 2.5 V with a sweep rate of ≈1 V s^{-1} are shown in **Figure 1**a. The voltage polarity is defined toward the Pt electrode and each group of curves consists of ten switching cycles. Measurements on two different device sizes of $(60\ nm)^2$ and $(500\ nm)^2$ are indicated by bright and dark colors, respectively. The orange and red switching hysteresis show a gradual SET behavior which results when the devices were cycled starting from their insulating initial states, i.e., without prior electroforming. The *I–V* curves with gradual SET and gradual RESET events exhibit a low variability of the resistance states, consistent with the results reported in Refs. [32,33]. The SET process is observed when a positive voltage signal is applied to the Pt Schottky electrode, while a negative voltage results in a RESET. Comparing the switching characteristics for the different device sizes, the shape of the *I–V* curves is not affected, but the total current decreases significantly for the smaller devices. Quantitative analysis of the area dependence of the read values for the *a*-HRS and *a*-LRS taken at −0.5 V is shown by the red symbols in Figure 1b, which include results from ten devices and 200 cycles each. A perfect area scaling is confirmed by the red dashed lines fitted to the data points with a slope of minus one in the plot (log *R*) versus (log *A*). The small standard deviation of the mean values indicates low variability from device to device and from cycle to cycle. The stability of the area-dependent states for at least $6 \cdot 10^4$ s at room temperature was confirmed by retention measurements shown in Figure S1 (Supporting Information). In addition, the reproducibility of the switching over 300 cycles is shown in Figure S2 (Supporting Information).

In contrast, after an initial electroforming step at −3.5 ± 0.3 V with a current compliance of 400 µA, represented by the grey lines in Figure 1a, the 1st RESET is achieved by applying a positive voltage to the Pt electrode. Subsequently, abrupt SET and gradual RESET events occur when a negative and a positive voltage is applied, respectively. This behavior, represented by the blue curves in Figure 1a, corresponds to standard filamentary VCM-type switching. The reading values, *f*-HRS and *f*-LRS, which were

 © 2023 The Authors. Advanced Electronic Materials published by Wiley-VCH GmbH

ADVANCED ELECTRONIC MATERIALS
Open Access
www.advelectronicmat.de

2199160x, 2023, 12, Downloaded from https://onlinelibrary.wiley.com/doi/10.1002/aelm.202300520, Wiley Online Library on [11/12/2023]. See the Terms and Conditions (https://onlinelibrary.wiley.com/terms-and-conditions) on Wiley Online Library for rules of use; OA articles are governed by the applicable Creative Commons License

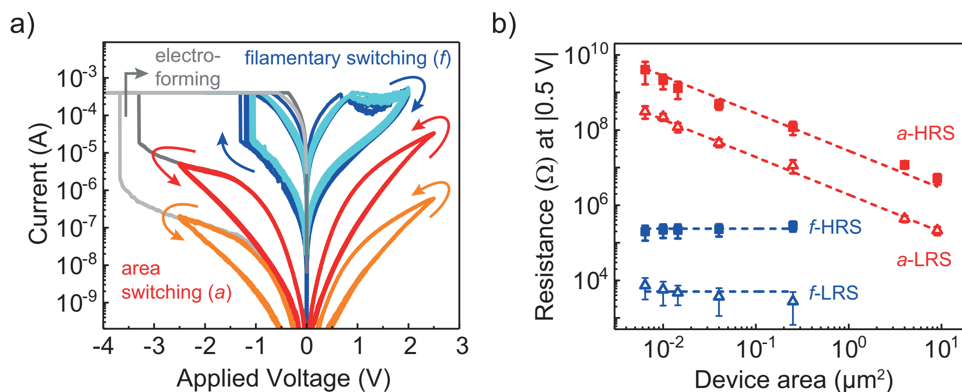

Figure 1. a) Filamentary switching for (500 nm)^2 in dark blue and (60 nm)^2 in light blue and area switching for (500 nm)^2 in red and (60 nm)^2 in orange for Pt/1.2 nm Al_2O_3/7 nm TiO_x/Cr/Pt (bottom to top) ReRAM devices. Voltage polarity is defined toward the Pt bottom electrode with ground potential at the top electrode. b) Area dependence of the resistance states for filamentary (*f*) and area (*a*) switching read at |0.5| V in the respective RESET polarity. The dashed lines represent linear fits to the data with a slope of zero and minus one for the *f*– and *a*–states, respectively. The error bars indicate the scattering of the read values over 50 cycles for each state.

determined for devices with different area that were switched with the same operation parameters are shown as blue symbols in Figure 1b. The dashed horizontal blue lines fitted to the data points with a slope of zero emphasize that the resistance states in the filamentary mode are almost independent of the device area. Therefore, the two switching modes shown in red and blue will be discussed further as area (*a*-) mode and filamentary (*f*-) mode, respectively.

2.1.2. Potentiation and Depression Behavior

In neuromorphic computing potentiation and depression properties describe the weight change of an artificial synapse by application of trains of voltage pulses. To evaluate the potentiation/depression behavior of the device in this study when operated in the different modes, successive voltage pulses with constant pulse amplitude and a pulse width of 1 ms were applied and the conductance state was read after each pulse. Devices with an electrode area of (500 nm)^2 were selected for this study. The sequence of programming and reading pulses for the area switching device is shown in **Figure 2**a above. For potentiation, 200 consecutive pulses of +2.2 V were applied. The conductance of the device was measured after each pulse by applying a read pulse of −1.0 V and 1 ms. For depression, 200 pulses of −2.2 V were applied, and the conductance state was read in the same manner as before. The resulting conductance for three representative cycles of potentiation and depression, shown in the

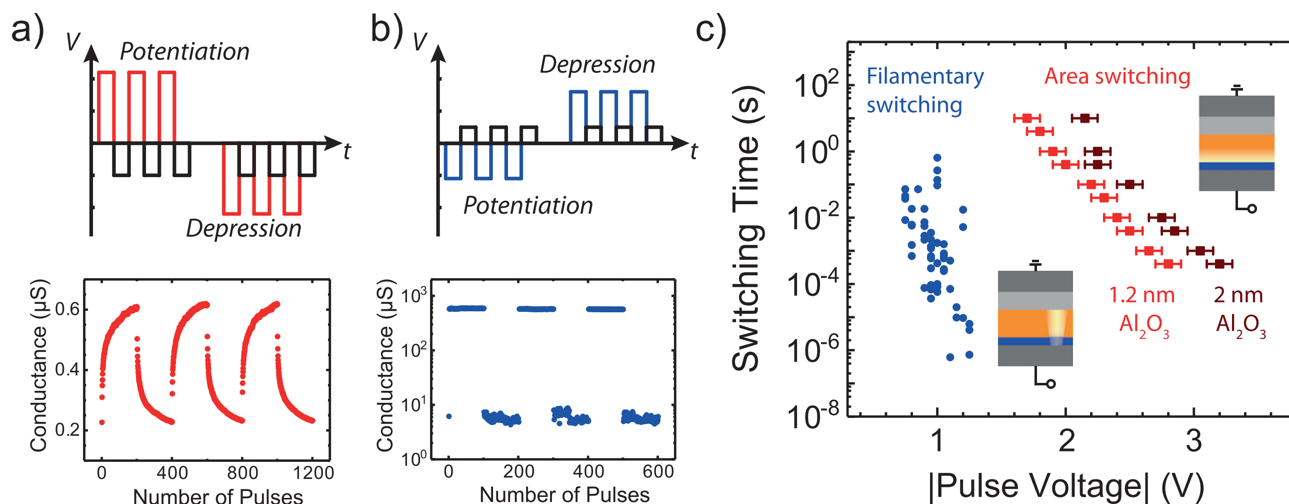

Figure 2. Conductance of the device as a function of the number of applied pulses for a) the area mode and b) filamentary mode with the pulse delivery scheme performed to evaluate the synaptic plasticity of the structure. c) Logarithmic time-voltage relationship of the SET event. The filamentary mode (blue) shows a faster SET time with reduced pulse voltage associated with high variability of the switching times compared to the area mode, which requires higher voltages and longer pulses for device with the same Al_2O_3 thickness of 1.2 nm (red) to obtain a resistance ratio of five. The switching speed is further decreased for devices with increased Al_2O_3 thickness of 2 nm (dark red). The insets show the device stacks from the bottom to top: Pt (grey) / Al_2O_3 (blue) / TiO_x (yellow) / Cr (light grey) / Pt (grey), and the bright yellow color indicates the switching mode being either filamentary or area dependent.

© 2023 The Authors. Advanced Electronic Materials published by Wiley-VCH GmbH

2199160x, 2023, 12, Downloaded from https://onlinelibrary.wiley.com/doi/10.1002/aelm.202300520, Wiley Online Library on [11/12/2023]. See the Terms and Conditions (https://onlinelibrary.wiley.com/terms-and-conditions) on Wiley Online Library for rules of use; OA articles are governed by the applicable Creative Commons License

lower plot of Figure 2a, demonstrate gradual resistance change for the area switching device. However, this change is not linear, but shows a saturation-like behavior with a stronger conductance change triggered by the first pulses of the two series. Similar behavior has been described as soft-bound behavior[35–37] and non-symmetric switching characteristics, since the conductance increases and decreases are not equal in magnitude and both have different dependencies of the conductance of the device. Recently, researchers at IBM Research AI have successfully demonstrated neural network training on arrays consisting of such non-symmetric devices using a new algorithm called "Tiki-Taka".[38] Following this approach, Al_2O_3/TiO_x-based device operated in area mode show promise for neuromorphic computing (NC) applications.

The sequence of programming and reading pulses applied to the filamentary switching device is shown in Figure 2b above. For potentiation and depression, 100 consecutive pulses of −1.1 V were applied with 400 µA compliance current and +1.6 V, respectively. The readout pulse was + 0.5 V and 1 ms. The conductance measured for three consecutive cycles is shown in the graph below. With the first potentiation pulse, the conductance jumps to the final high conductance defined by the external compliance. With the first depression pulse, the conductance returns to the low conductance, with some variability occurring with repeated pulses. For the given operation parameters, the behavior of the filamentary switched $Pt/Al_2O_3/TiO_x/Cr/Pt$ device is characterized by abrupt SET and RESET events. For Al_2O_3/TiO_x-based devices operated in the filamentary mode the switching stochasticity might be utilized to emulate an artificial synapse using multiple ReRAM cells according to.[39] Following the intention of this study, which is the comparison of the two switching modes in the same device, the analysis is performed for a programming time of 1 ms that is close to the timing of biological events. However, it should be mentioned that rather linear potentiation/depression characteristics can also be realized in filamentary switching devices if the pulse width meets the transition time of the switching event.[40,41]

2.1.3. SET Switching Kinetics

The dependence of the switching rate on the voltage and temperature distribution in the ReRAM cell is controlled by the rate-limiting step of the switching kinetics. It is widely accepted, that in conventional filamentary memristive devices, positively charged oxygen vacancies in the transition metal oxide layer are attracted toward the negatively biased Schottky electrode, increasing their concentration in the gap region between the conducting filament and the Pt active electrode. A significant increase in local temperature due to Joule heating accelerates this ion migration, resulting in extremely nonlinear SET kinetics in filamentary devices.[34,42] The standard *f*–mode is therefore considered as reference for analyzing the SET kinetic behavior of the *a*–mode with opposite switching polarity. For this mode, a switching mechanism based on an area-dependent interfacial exchange reaction of oxygen near the Pt active electrode combined with ion migration is discussed.[17,43–45] Despite different approaches, a direct comparison of the switching kinetic behavior for the two different modes, namely, the "abrupt, filamentary" and the "gradual, interfacial" is difficult, because often devices of different dimensions and various layer stacks are used for either case. Here, the SET kinetic behavior of identical devices was measured on the same sample and is discussed below. The standard filamentary SET event is characterized by an abrupt current rise in response to a voltage pulse of sufficient amplitude and width. In measurements of transient current response, the delay time between the voltage applied and the current rise is often defined as the SET time.[46] In contrast, gradual SET events show a continuous current increase for a given voltage pulse. In this case, SET events are typically classified according to how long it takes to reach a defined conductance when a specific voltage pulse was applied.[31,40] The obtained SET kinetic behaviors for devices of size $(500\ nm)^2$ in terms of semi-logarithmic relationships between time and voltage are shown in Figure 2c. The filamentary devices were programmed into an *f*-HRS in the range of (80 ± 30) kΩ before the SET pulse was applied. The SET times were derived from these transient current responses, which showed current increase of at least a factor of ten. The SET times of the area switching devices were determined from the widths of voltage pulses that changed the resistance value of the device read at −0.5 V by a factor of five. The width of the voltage pulses was changed in discrete steps, and for each pulse width the pulse amplitude was increased until the required resistance change was obtained. The statistical variation of the voltage that causes the required resistance change for the given pulse width is considered by the error bars added to the switching kinetic data of the *a*-type devices. In contrast, the stochasticity of the SET event for the *f*-type devices is reflected by the cloud of blue data points. Before the experiment, the devices were switched 200 times using voltage pulses of alternating voltage of ± 2.0 V and 1 s pulse duration each. The *a*-mode devices were programmed into a defined *a*-HRS in the range of (200 ± 20) MΩ before the defined SET pulse was applied. RESET pulses of 1 s duration and increasing voltage amplitude were then applied when the resistance of the cell was below the defined *a*-HRS value.

The plot of the SET kinetics in Figure 2c clearly shows that the *f*-mode (blue) enables faster SET events at lower voltages compared to the *a*-mode (red). Choosing the identical pulse length, a gradual SET event in *a*-mode requires about twice the voltage as an abrupt SET event in *f*-switching. According to the physical understanding of *f*-switching, the current through the device is highly concentrated in the filament region and therefore, the local current density can easily exceed the current density of *a*-switching devices by orders of magnitude. Consequently, the fast switching in filamentary devices is due to the current-induced Joule heating and temperature-accelerated drift and diffusion of oxygen vacancies caused by the high current density in the filamentary region. Devices switched in *a*-mode with lower current density for this reason, require voltage pulses with much higher amplitude to achieve a SET event at the same time as *f*-switching. Increasing the thickness of the Al_2O_3 tunneling barrier from 1.2 nm (red symbols) to ≈2 nm (dark red symbols) further shifts the SET kinetics curve to higher voltages. The SET kinetics for the *f*-mode agrees well with the temperature-accelerated drift and diffusion model of oxygen vacancies.[42] In contrast, the SET kinetics of the $Pt/Al_2O_3/TiO_x/Cr/Pt$ devices switched in *a*-mode is determined either by a field-driven exchange of oxygen ions across the interface near the Pt active

© 2023 The Authors. Advanced Electronic Materials published by Wiley-VCH GmbH

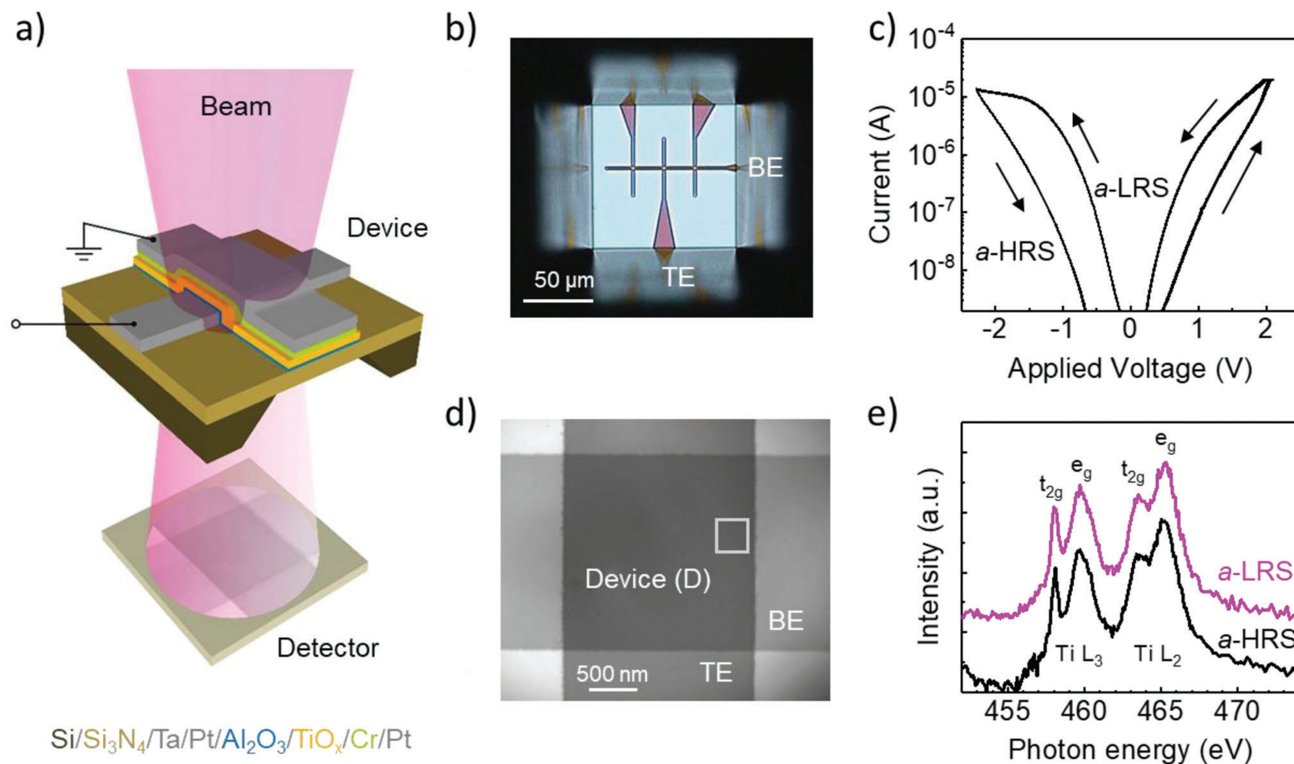

Figure 3. a) Illustration of the device geometry for transmission X-ray spectromicroscopic characterization with a crossbar device on the free-standing 40 nm thick Si_3N_4 membrane. b) Microscope image of the device structure taken in transmission from the backside of the Si substrate through the Si_3N_4 membrane window. The probe pads are outside the membrane. c) Electrical characterization of the Pt/Al_2O_3 (1.5 nm)/TiO_x (7 nm)/Cr/Pt cell taken prior to the spectromicroscopic analysis. The device of 2 µm x 2 µm size shows the typical area switching with a RESET into *a*-HRS and a SET into *a*-LRS obtained for a voltage of negative and positive polarity applied to the Pt Schottky electrode, respectively. d) TXM image of the device set to *a*-LRS taken at the Ti L-edge at a photon energy of 459.1 eV. e) Ti L-edge absorption spectra extracted from the energy image series of a device area defined by the grey square for the device set to the *a*-LRS (pink) and to the *a*-HRS (black).

electrode or by ion movement in the Al_2O_3 interlayer, depending on which process becomes the rate-determining step (RDS). The latter has been identified by Siegel et al. as RDS for the SET events in interfacial switching $SrTiO_3$/interlayer/Pt devices, while oxygen ion exchange at the interlayer/Pt interface is still assumed.[17] In contrast to the amorphous films obtained by atomic layer deposition in this study, the epitaxial $SrTiO_3$ thin films were grown by pulsed laser deposition. In such devices, nanoscale conducting filaments were identified by scanning transmission electron microscopy and core-loss spectroscopy.[47] To obtain structural information about the devices compared in this study, spectroscopic studies were performed, which are explained and discussed below.

2.2. Spectroscopic Investigations

2.2.1. Transmission X-Ray Microscopy (TXM)

For the near-edge X-ray absorption fine structure (NEXAFS) TXM measurements, the total thickness of the sample was reduced to less than 100 nm to obtain a reasonable signal-to-noise ratio. For this purpose, the stack itself was set to Ta (3 nm)/Pt (15 nm)/Al_2O_3 (1.5 nm)/TiO_x (7 nm)/Cr (5 nm)/Pt (15 nm) (from bottom to top) and the cross bars were fabricated on Si substrates with a 40 nm thick Si_3N_4 layer on top. The sample setup for TXM characterization is schematically shown in **Figure 3**a. The bottom and top lines are 2 µm wide and three crossbar devices are positioned on the free-standing Si_3N_4 membrane obtained after etching a defined window into the Si substrate from the backside (see Figure 3b). Recent studies have shown that ReRAM devices on freestanding Si_3N_4 membranes are sensitive to breakdown at lower voltages compared to devices on Si bulk wafers.[48,49] Therefore, the "TXM-devices" were fabricated with a slightly increased Al_2O_3 thickness of 1.5 nm.

Devices Switched in Area Mode: Figure 3c shows several area switching cycles measured for the device under study prior to the spectromicroscopic analysis. The switching curves are superimposed, indicating little variability from cycle to cycle. From the recorded *I–V*-curves, a typical *a*-type switching is evident. As a precaution, the maximum voltage for RESET and the maximum current for SET were limited to −2.3 V and 200 µA, respectively. Under these conditions, stable reversible bipolar switching was achieved between *a*-LRS and *a*-HRS with resistance values of ≈450 kΩ and 30 MΩ, respectively, measured at a read voltage of −1.0 V. TXM measurements were performed on two devices, and each device was programmed two times into the *a*-HRS and the *a*-LRS before subsequent TXM data acquisition. In this way, a total of four TXM images was taken for each condition. Figure 3d shows a representative TXM image of a device in *a*-LRS

© 2023 The Authors. Advanced Electronic Materials published by Wiley-VCH GmbH

2199160x, 2023, 12, Downloaded from https://onlinelibrary.wiley.com/doi/10.1002/aelm.202300520, Wiley Online Library on [11/12/2023]. See the Terms and Conditions (https://onlinelibrary.wiley.com/terms-and-conditions) on Wiley Online Library for rules of use; OA articles are governed by the applicable Creative Commons License

2199160x, 2023, 12, Downloaded from https://onlinelibrary.wiley.com/doi/10.1002/aelm.202300520, Wiley Online Library on [11/12/2023]. See the Terms and Conditions (https://onlinelibrary.wiley.com/terms-and-conditions) on Wiley Online Library for rules of use; OA articles are governed by the applicable Creative Commons License

measured at a photon energy of 459.1 eV. The 2 µm × 2 µm size cross-junction device area with the BE and TE lines can be clearly distinguished due to the difference in total absorption, which is due to differences in the layer stacks and thicknesses (see Figure 3a for details). The layer stack below the TE appears darker because TiO_x absorbs strongly at this photon energy. All four TXM images of the devices in *a*-LRS were carefully analyzed. However, in none of the images for the devices in *a*-LRS could a difference in local intensity be detected that could have indicated local valence changes of TiO_x corresponding to preferred current paths. Therefore, the possibility of multiple conducting filament scenario as reported in [50] and [51] is considered unlikely for the $Pt/Al_2O_3/TiO_x/Cr/Pt$ devices of this study. This is true for a diameter of the localized conducting filament larger than ≈30 nm. The TXM results agree well with the area switching behavior in the $Pt/Al_2O_3/TiO_x/Cr/Pt$ devices observed without an electroforming step.

By extracting NEXAFS spectra from energy image series acquired by TXM, chemical identification of the species can be performed. For the device programmed in *a*-LRS and *a*-HRS, Figure 3e shows representative spectra in pink and black, respectively, taken from the region marked by the grey square in Figure 3d. Both spectra show the typical Ti-L edge absorption caused by the excitation of electrons from the 2p to the 3d level. Four well-separated main lines are observed, which are due to the spin-orbit splitting into L_2 and L_3 lines and the crystal-field splitting into t_{2g} and e_g lines in octahedral symmetry. The absorption spectrum of the Ti-L edge shows distinct features for the different phases of stoichiometric TiO_2, reduced TiO_{2-x}, and Magnéli phases Ti_nO_{2n-1} ($n > 2$).[52] Comparison with literature reveals good agreement of both spectra with the amorphous and anatase TiO_2 phase. Characteristically, the spectral features are broad and smooth with a higher intensity of the (Ti L_3, e_g) peak compared to the (Ti L_3, t_{2g}) peak. However, the differences between amorphous and anatase TiO_2 are subtle. The crystalline phase shows sharper absorption peaks, this means an increased first (Ti L_3, t_{2g}) and third (Ti L_2, t_{2g}) main peak (at 458 and 463 eV), as well as stronger crystal field splitting compared to the amorphous structure. In addition, for anatase TiO_2 a striking splitting of the second main peak ((Ti L_3, e_g) at 460.5 eV) is expected due to a distortion of the Ti site from octahedral to tetragonal symmetry.[53,54] Such features are observed in the spectra in Figure 3e, although slightly attenuated. This indicates high structural disorder, as expected for amorphous TiO_x. Therefore, we assign the chemical nature of the TiO_x layer in the area switching $Pt/Al_2O_3/TiO_x/Cr/Pt$ devices to amorphous TiO_x with a small contribution from the anatase phase. This result agrees well with previous structural analyses of TiO_x thin films grown by a thermal ALD process from TDMAT and H_2O using X-ray diffraction and grazing incidence total X-ray scattering in combination with pair distribution function analysis.[55] The spectra shown in Figure 3e don't reveal any clear differences between the *a*-HRS and *a*-LRS of the device. Minor deviations are caused by slight variations of the experimental conditions during a measurement. Moreover, no differences can be observed between the spectra from the device region and from the region below the top electrode, which is the reference for the deposited $Al_2O_3/TiO_x/Cr/Pt$ layer stack. In total, the NEXAFS spectra extracted from the energy image series acquired by TXM do not show any characteristic features that could be assigned to one of the two resistance states, *a*-LRS or *a*-HRS, of the area switching process. There were no measurable structural changes in the TiO_x film when the device was switched in the *a*-mode. The consistent conclusion is that the TiO_x film remained in its amorphous as-deposited state during *a*-switching of the device. Considering a crystallization temperature of the TiO_x film of ≈670 K it is summarized that no strong Joule heating can be involved in the *a*-switching process.

Devices Switched in Filamentary Mode: For comparison, also *f*-switching devices have been analyzed. All samples for TXM investigation were fabricated in the same way as before. The only difference in device operation is the electroforming step applied prior to the typical *f*-switching, which for the device of this TXM study is shown in **Figure 4**a), with values of the *f*-HRS and *f*-LRS at 0.5 V being ≈90 and 6 kΩ, respectively. The TXM measurements were performed operando. Figure 4b shows a representative TXM image of the device in *f*-LRS for a photon energy of 459.1 eV. The film thickness and elemental mass have a strong effect on the attenuation of the signal due to absorption. Therefore, the cross junction, the BE and TE layers, and the pure Si_3N_4 membrane outside of the device can be clearly identified from the different grey tones. On the right side of the vertically extending TE is a vertical bar that has slightly darker grey tones than the BE and Si_3N_4 membrane that follow to the right. Additional analysis by electron microscopy revealed that this vertical bar consists of TiO_x material left over after etching the TE due to non-ideal vertical side walls. For the TXM analysis, this imperfect structuring allows interesting observations because it provides information about a TiO_x film that is close to the cross junction but was not exposed to an electric field due to the lack of TE. Chemical analysis is performed using NEXAFS spectra extracted from energy image series acquired by TXM. In addition, principal component analysis (PCA) suggests dividing the device into three distinct components, the local distribution of which is shown in Figure 4c–e. The figures show the region near the lower right corner of the device. The first component (green) represents the average TiO_x layer in the whole area of the device, abbreviated by "D". Figure 4c shows that this component is evenly distributed up to the edges of the crossbar junction. The second component (blue) appears mainly in a region of ≈1 µm in diameter near the lower right corner of the device (see Figure 4d)). The third component (pink) shows a strong contrast locally limited to an area with a diameter of ≈50 nm (see Figure 4e). Data from the corresponding regions, i.e., device "D", halo "H", and filament "F" (see Figure 4b), were extracted to obtain the X-ray absorption spectra and identify the specific phases. The corresponding Ti absorption spectra in Figure 4f show significant variations. The green spectrum is representative of device region "D" as well as portions of the remaining TiO_x on the TE sidewall. This spectrum corresponds to the TiO_x amorphous phase and is very similar to the spectrum shown in Figure 3e for the device immediately after fabrication.

Characteristic features are the broad and smooth spectral features, a higher intensity of the (Ti L_3, e_g) peak compared to the (Ti L_3, t_{2g}) peak, and the absence of the splitting of the (Ti L_3, e_g) peak. In contrast, the blue spectrum extracted from the blue rectangle inside the larger circular halo-like "H" region and outside the TE shows typical features of crystalline TiO_2, especially a slight broadening of the (Ti L_3, e_g) peak, indicating distortion

© 2023 The Authors. Advanced Electronic Materials published by Wiley-VCH GmbH

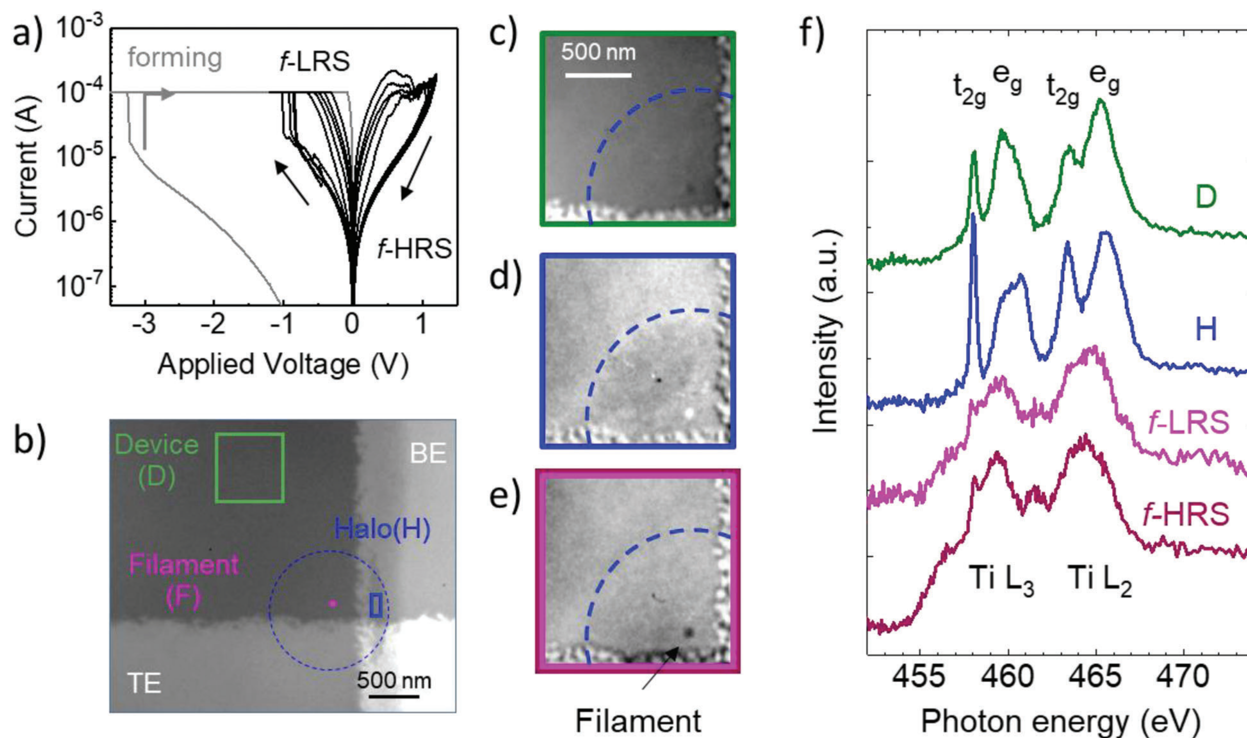

Figure 4. a) Electrical characterization of the Pt/Al_2O_3/TiO_x/Cr/Pt cell before spectroscopic measurements. After electroforming, the device shows typical filamentary VCM-type switching. b) TXM image of the device in *f*-LRS acquired at the Ti L-edge at a photon energy of 459.1 eV. c–e) Components maps at the Ti L-edge enabling the identification of regions of amorphous TiO_x, rutile-type TiO_2 and reduced TiO_{2-x}. f) Near-edge X-ray absorption fine structure (NEXAFS) spectra of the different locations (marked in b) of the titania layer in the filamentary switching ReRAM device, recorded at the Ti L_{23} edge. The ranges of the t_{2g}- and e_g-related peaks at the L_3 and L_2 edge are indicated.

of the TiO_6 octahedron.[56] Based on the broadened peak shape, the respective type of octahedral distortion and thus the phase of the TiO_2 can be distinguished. Here, the peak has a shoulder at lower energy, which is typical for the rutile phase of TiO_2 with tetragonal distortion of the TiO_6 octahedron.[57,58] Furthermore, the intensity of the (Ti L_3, t_{2g}) peak compared to the (Ti L_3, e_g) is stronger. Spectra from different regions inside the halo "H" are compared in Figure S3a–c (Supporting Information). Summarizing, region "H" can be clearly assigned to rutile-type TiO_2 phase. The pink and the purple spectrum from the filamentary region "F" in Figure 4b differ clearly from the other two spectra. In addition to a significant shift of the broad Ti $L_{2,3}$ peaks toward lower photon energy, new features appear ≈456 and 461.5 eV. This is consistent with the presence of a partially reduced phase containing Ti^{3+}.[7] Even more pronounced is the merger of the crystal field-split doublet pairs (e_g and t_{2g}), indicating lower local symmetry. A mixed valence composition of Ti^{3+} and Ti^{4+} exhibits broader features compared to pure Ti^{4+} phases, which can be attributed to core shifts of the Ti^{3+} levels as well as overlap and increasing number of allowed transitions in the Ti^{3+} phases.[59,60] Therefore, region "F" can be assigned to reduced titanium oxide. Comparison with spectra reported in the literature for the different TiO_x and Ti_nO_{2n-1} ($n > 2$) phases[53] leads to the conclusion that the pink and purple spectrum in Figure 4f are close to that of the Ti_4O_7 phase. Spectra of the filament region were measured for the device switched into *f*-LRS (pink) and *f*-HRS (purple). However, due to the small volume of the filament region and the low signal-to-noise ratio which is due to the small area of only 9 image pixels from which the spectrum was extracted, no robust differences could be identified for the different resistance states. In addition, attention should be paid to the area size of the different regimes. Filament "F" of reduced TiO_{2-x} phase is confined to a region of ≈50 nm diameter surrounded by a region "H" of rutile-type TiO_2 of ≈1 µm diameter. No additional features were detected for this 4 µm^2 device made of an amorphous TiO_x layer ("D"). The electroforming process, which the device has been subjected to prior to the filamentary switching, is understood as a soft local breakdown event characterized by increased electronic current, local heating and an increased oxygen ion drift and diffusion in the heated regime and under the applied electric field. Under these conditions, a local conductive filament is formed in the amorphous TiO_x matrix. For filament formation, a negative voltage was applied to the active Pt electrode and the Cr top electrode was grounded (see Figure 4a). Under the electric field, positively charged oxygen vacancies form near the Cr electrode and drift toward the Pt electrode. This proves to be a self-accelerating process, as the current-induced Joule heating makes an additional contribution. The observed structural features shown in Figure 4 illustrate the result of this process, which consists of a ≈50 nm size filament from reduced titanium oxide surrounded by crystallized rutile-type TiO_2 with a diameter of ≈1 µm. In previous annealing studies of the amorphous TiO_x films grown by thermal ALD crystallization into the rutile phase was obtained at temperatures ≈670 K. For this, it can be inferred

 © 2023 The Authors. Advanced Electronic Materials published by Wiley-VCH GmbH

2199160x, 2023, 12, Downloaded from https://onlinelibrary.wiley.com/doi/10.1002/aelm.202300520, Wiley Online Library on [11/12/2023]. See the Terms and Conditions (https://onlinelibrary.wiley.com/terms-and-conditions) on Wiley Online Library for rules of use; OA articles are governed by the applicable Creative Commons License

2199160x, 2023, 12, Downloaded from https://onlinelibrary.wiley.com/doi/10.1002/aelm.202300520, Wiley Online Library on [11/12/2023]. See the Terms and Conditions (https://onlinelibrary.wiley.com/terms-and-conditions) on Wiley Online Library for rules of use; OA articles are governed by the applicable Creative Commons License

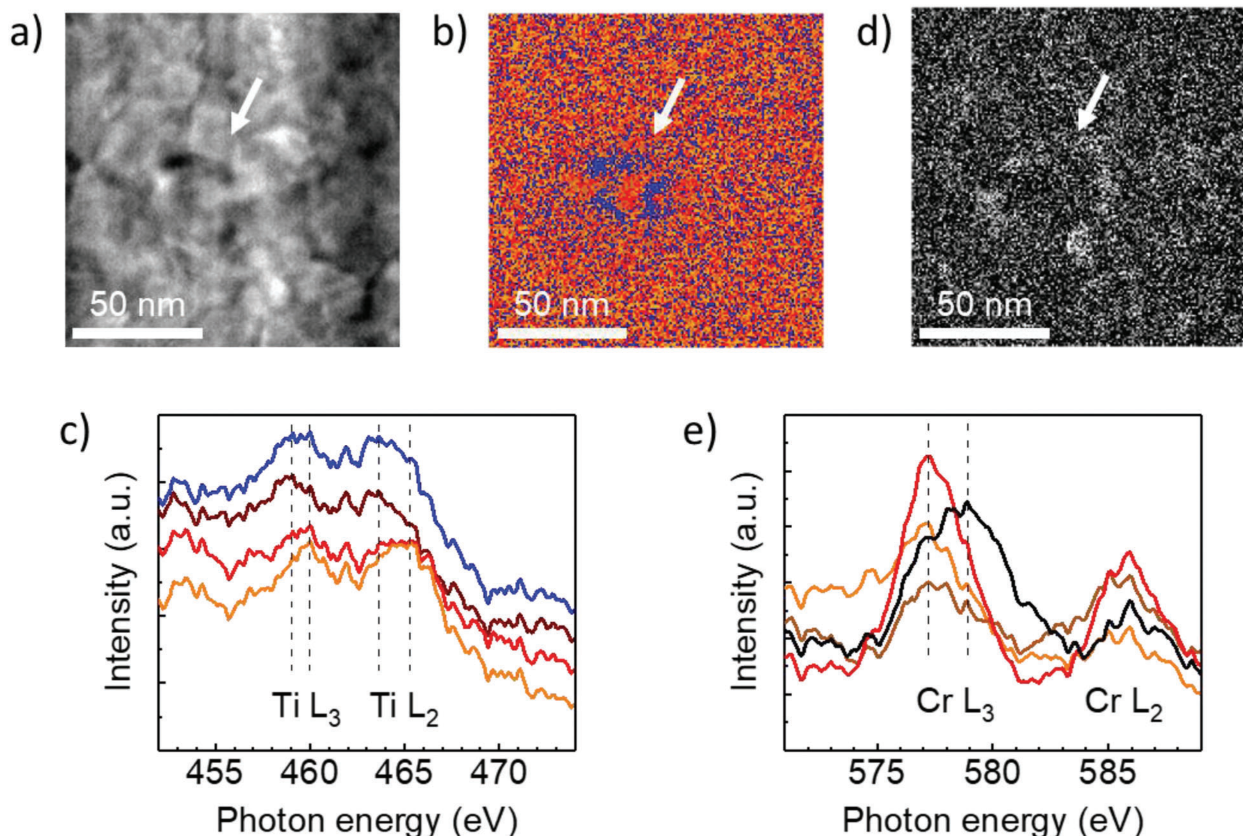

Figure 5. a) HAADF-STEM image of the filamentary switched Pt/Al_2O_3/TiO_x/Cr/Pt device taken in a regime of ≈120 nm × 120 nm around the conductive filament. b) Color-coded spatial distribution map of the four components of the Ti L-edge which are determined by means of non-negative matrix factorization (NMF) and clustering analysis and c) the four corresponding Ti L-edge component spectra. d) Spatial distribution map of the CrO_x signal corresponding to the black spectrum shown in e), which is obtained after the decomposition of the components at the Cr L-edge. In this spatial map of a single component, dark and light grey colors represent low and high concentrations, respectively. e) Cr L-edge component spectra obtained by NMF and clustering. The three components orange, red and brown refer to metallic chromium, while the shifted peak of the component drawn in black corresponds to chromium oxide.

that the area "H" surrounding the filament "F" was exposed to temperatures higher than this by dissipating the heat generated during the electroforming event. Equivalent results have been reported by Meng et al. for TaO_x.[61] Here, the even stronger crystallization observed at the edge of the TE where the TiO_x was not covered by the Pt TE is understood from a slower heat dissipation due to reduced heat transport.

2.2.2. Scanning Transmission Electron Microscopy (STEM-EELS)

Devices Switched in Filamentary Mode: The device programmed into the *f*-LRS was also chemically analyzed by STEM combined with electron energy loss spectroscopy (EELS), which provides a higher spatial resolution compared to TXM and further enables the chemical analysis of the chromium oxidation state. **Figure 5**a shows the high-angle annular dark-field (HAADF)-STEM image of the filamentary regime "F" with its surrounding, which is basically the "H" region (cf. Figure 4b,e). Despite the overlapping granular microstructure of the Cr/Pt TE, a slightly dark spot can be seen in Figure 5a (highlighted by the white arrow), indicating microstructural changes in the device. Here, non-negative matrix factorization (NMF) followed by clustering was used to decompose the distinct spectra from the noisy EELS map for each local position in the HAADF-STEM image. In total, four components were identified, and the resulting color-coded distribution map of the four decomposed components of the Ti L-edge is shown in Figure 5b. The corresponding Ti L-edge spectra in their respective color are shown in Figure 5c. Due to the limited energy resolution of EELS measurements, the crystal field-split doublet pairs (e_g and t_{2g}) cannot be resolved. However, the peaks representing the merging of the e_g and t_{2g} peaks also show a significant shift in the four components. From Figure 5b, it appears that the region outside the filament (i.e. "H") is dominated by the orange and red components, which have peak maxima at higher electron loss energies corresponding to a higher titanium valence state compared to the brown and blue components. This agrees well with the results of TXM analysis, which identifies a rutile-type TiO_2 phase in the "H" region near the filament. The filament region itself (marked by the white arrow in Figures 5a,b,d is dominated by the blue and brown components characterized by peaks at lower electron loss energies corresponding to reduced TiO_{2-x}, also in agreement with the TXM results. From the HAADF-STEM image (Figure 5a) combined

 © 2023 The Authors. Advanced Electronic Materials published by Wiley-VCH GmbH

with the component analysis map (Figure 5b) the diameter of the conductive filament is confirmed to be slightly smaller than ≈50 nm.

In addition, the Cr L-edge of the Pt/Al_2O_3/TiO_x/Cr/Pt device was investigated and analyzed by the same method applied to Ti L-edge. Figure 5d shows the spatial intensity distribution map for one component that corresponds to the black spectrum in Figure 5e. In the spatial distribution a high and low amount is represented by brighter and darker grey color, respectively. From the comparison of the spatial distribution maps in Figure 5b,d it is visible that an increased amount of the chromium compound corresponding to the black spectrum in Figure 5e is located at the outer periphery of the filament perimeter. Figure 5e displays the four components which were identified for the Cr L-edge. The red, orange, and brown spectra can be correlated to Cr metal, with the maximum of the L_3 and L_2 peaks at 577.5 and 586.0 eV, respectively, in agreement with the literature.[62] Again, the minor differences between these components can be attributed to differences in microstructure such as thickness of the remaining top electrode. In contrast, the black component shows a clear shift of 1 to 2 eV to higher binding energies and corresponds to a higher chromium valence state equivalent to a signature of CrO_x. The increased intensity of this compound at the edge of the filament's perimeter can be attributed to the electroforming and filamentary switching process: The oxygen vacancy formation in the TiO_x layer close to the Cr electrode is due to an oxygen ion transfer from the TiO_x to Cr, resulting in chromium oxide.

Nanoscale chemical analysis using TXM, and STEM clearly shows a filamentary region formed in a Pt/1.5 nm Al_2O_3/7 nm TiO_x/Cr/Pt device of 2 µm × 2 µm size after an electroforming process and filamentary resistive switching. The filament with a diameter slightly smaller than ≈50 nm is surrounded by rutile-like TiO_2 with a diameter of ≈1 µm. Signatures of CrO_x are observed in the Cr electrode adjacent to the TiO_x layer laterally confined to the outer perimeter of the TiO_{2-x}-based conductive filament. The spectromicroscopic analysis uncovers microstructural and -chemical changes of the device stack which are attributed to effects of local Joule heating caused by the high current density in the filament region. This proves that temperature accelerated local oxygen ion transfer from the TiO_x switching layer to the Cr oxygen exchange electrode is an important process accompanying the filament formation step. It should be noted that the observed local changes are mainly of chemical and structural nature, with very little morphological impact. In contrast to the filamentary mode, neither local nor lateral chemical changes were observed in the area switching device, where the TiO_x film remained in its amorphous state as it was deposited. The area switching mode is therefore further analyzed in terms of the electronic conduction mechanism.

2.3. Electronic Conduction Mechanism

From previous work on *f*-switching Pt/TiO_x/Ti/Pt devices, it is known that electronic transport occurs via the conduction band due to the shallow defect states of the oxygen vacancies in TiO_x.[63] The resistive switching in these devices is an effect of the change in tunnel distance due to a variation in oxygen vacancy concentration causing different Schottky barrier screening lengths.[32,64] In this study, the area-dependent switching of Pt/Al_2O_3/TiO_x/Cr/Pt bilayer devices is investigated. The oxide double layer device consists of a 1.2 nm thick Al_2O_3 and a 7 nm TiO_x layer, which serve as tunneling barrier and n-type semiconductor, respectively. The insulating properties of the Al_2O_3 film by PE-ALD and the semiconducting behavior of the TiO_x film by thermal ALD have been demonstrated in previous studies.[65,66] However, the open structure of the γ-alumina phase still allows exchange of oxygen ions across the Al_2O_3/TiO_x boundary as well as oxygen ion diffusion through the Al_2O_3 thin layer.[63] The area scaling of the resistivity values for the pristine state and for *a*-LRS and *a*-HRS (see Figure 1b) shows that the conductivity can be averaged over the device area, which allows a continuous description of the electronic transport. Thus, a model system is constructed from the exact material stack, namely, a high work function Pt electrode, a 1.2 nm Al_2O_3 tunneling barrier, a 7 nm thick semiconducting TiO_x layer, with the voltage applied to the Pt electrode. This layer stack can be considered as a metal-oxide-semiconductor (MOS) capacitor, which allows the energy bands to be described analogous to a MOS capacitor in depletion mode, e.g., ref. [67]. The screening charge in the TiO_x layer is calculated as

$$Q_{\mathrm{TiOx}} = A_{\mathrm{cell}}\sqrt{2\varepsilon_0\,\varepsilon_{r,\mathrm{TiOx}}\,2\,[\mathrm{V_O}]\quad\psi_s} = A_{\mathrm{cell}}\,\beta\sqrt{\psi_s} \tag{1}$$

with the cell size A_{cell}, the vacuum permittivity ε_0, the relative permittivity of the semiconducting material $\varepsilon_{r,TiOx}$, the concentration of two times positively charged oxygen vacancies $[V_O]$, and the energy ψ_s at the interface between Al_2O_3 and TiO_x. Due to charge accumulation according to Equation (1), the Al_2O_3 film acts as a capacitor dielectric with a capacitance of

$$C_{\mathrm{Al_2O_3}} = A_{\mathrm{cell}}\frac{\varepsilon_0\varepsilon_{r,\mathrm{Al_2O_3}}}{d_{\mathrm{Al_2O_3}}} \tag{2}$$

with the relative permittivity ε_{r,Al_2O_3} and the thickness $d_{Al_2O_3}$ of the Al_2O_3 layer.

The applied voltage V equals the sum of all contributions

$$V = \frac{(\phi_{\mathrm{Pt}} - \phi_{\mathrm{TiOx}})}{e} - \frac{Q_{\mathrm{TiOx}}}{C_{\mathrm{Al_2O_3}}} - \frac{\psi_s}{e} \tag{3}$$

where ϕ_{Pt} and ϕ_{TiOx} denote the work functions of the two electrodes and e the electron charge.

Solving Equations (1–3) for ψ_s leads to

$$\psi_s(V) = \left(-\frac{e\beta A_{\mathrm{cell}}}{2\,C_{\mathrm{Al2O3}}} + \sqrt{-eV + \phi_{\mathrm{Pt}} - \phi_{\mathrm{TiOx}} + \frac{e^2 A_{\mathrm{cell}}^2\,\beta^2}{4C_{\mathrm{Al2O3}}^2}}\right)^2 \tag{4}$$

with $\beta = \sqrt{2\,\varepsilon_0\,\varepsilon_{r,\mathrm{TiOx}}\,2[\mathrm{V_O}]}$.

From ψ_s the width of the depletion zone in the TiO_x is calculated by

$$d_{\mathrm{dp}}(V) = \frac{\beta\sqrt{\psi_s(V)}}{2\,[\mathrm{V_O}]\,e} \tag{5}$$

The potential drop is approximated as parabolic within the depletion zone d_{dp} (V) in the TiO_x layer and linear in the Al_2O_3 layer,

© 2023 The Authors. Advanced Electronic Materials published by Wiley-VCH GmbH

2199160x, 2023, 12, Downloaded from https://onlinelibrary.wiley.com/doi/10.1002/aelm.202300520, Wiley Online Library on [11/12/2023]. See the Terms and Conditions (https://onlinelibrary.wiley.com/terms-and-conditions) on Wiley Online Library for rules of use; OA articles are governed by the applicable Creative Commons License

whereby $V_{Al_2O_3} = Q_{TiO_x}/C_{Al_2O_3}$ denotes the total voltage drop in the Al_2O_3. The internal potential determines the bending of the conduction band E_C, but it requires consideration of the offset $E_{C,offset}$ in the conduction band at the interface between the two oxides, which is given by the difference in the oxides' electron affinities ($\chi_{Al_2O_3} - \chi_{TiO_x}$). In the following, the position $z = 0$ is set to the interface between Pt and Al_2O_3. This results in the description for conduction band at each voltage

$$E_C(z) = \begin{cases} E_t + \psi_s \cdot \frac{\left(z - d_{dp}(V) - d_{Al_2O_3}\right)^2}{\left(d_{dp}(V)\right)^2} & d_{Al_2O_3} < z < d_{dp} + d_{Al_2O_3} \\ E_t + \psi_s + E_{C,offset} - eV_{Al_2O_3} \cdot \frac{\left(d_{Al_2O_3} - z\right)}{d_{Al_2O_3}} & 0 < z < d_{Al_2O_3} \end{cases} \quad (6)$$

Here, E_t describes the position of the equilibrium Fermi-level. With the barrier defined, the current transport through tunneling can be calculated using the Tsu–Esaki-formalism

$$I = A_{\text{cell}} \cdot \frac{4\pi\, m_e\, e}{h^3} \int_{E_{min}}^{E_{max}} Tr(E) N(E)\, dE \quad (7)$$

with the electron mass m_e and Planck's constant h. The transmission probability is calculated from the Wentzel–Kramers–Brillouin (WKB) approximation

$$Tr(E) = \exp\left(-\sqrt{\frac{2\,\pi^2\, m_t}{h^2}} \int \sqrt{E_C(z) - E}\, dz\right) \quad (8)$$

The thermal activation at each energy E is given by the supply function $N(E)$, and m_t defines the electron tunneling mass.[68–70] From this, the oxygen vacancy concentration $[V_O]$ as state variable is fitted to the experimental data. All other input parameters are taken from literature values listed in **Table 1**.

To only examine the electronic transport in the experiments, it must be decoupled from the ionic motion, i.e., a change in $[V_O]$. Therefore, $[V_O]$ must be approximately frozen for the electrical characterization. This can be achieved by analyzing the electronic current with short voltage signals that are too short in time to trigger vacancy migration. This type of measurement is referred to as "extended *I–V*"-characterization.[75] The *I–V* half cycles shown by the solid lines in **Figure 6**a represent the RESET branches obtained from continuous *I–V* cycling of a $(500\ \text{nm})^2$ device switched in the area mode between 2.5 and −2.5 V for the SET and the RESET, respectively (see Figure 1a) for comparison). In addition, the *I–V* characteristic of the device in the *a*-LRS was probed by voltage pulses of 25 µs width which aren't sufficiently long to initiate further resetting of the device. The resulting "extended *I–V*" characteristics shown by the red dots in Figure 6a) represents the purely electronic current response of the device. Here the data points give the current values which result from averaging in the range from 10 to 15 µs for the applied voltage pulse. Figure 6b) summarizes the extended *I–V* characteristics for the device programmed into four different states, two *a*-LRS, namely, 700 kΩ and 2 MΩ, and two *a*-HRS, namely, 20 MΩ and 40 MΩ, shown by red squares, orange circles, grey triangles, and black triangles, respectively.

Table 1. List of the material parameters.

	TiO_x		Al_2O_3	Pt
d	7.0 nm		1.2 nm	
ε_r	8.0[71]		2.2[a)][72]	
m_t		$0.25 \cdot m_e$[73]		
E_t	0.1 eV[63]			
χ	3.9 eV[74]		2.6 eV[73]	
ϕ				5.84 eV[74]

a) for thin films of <2 nm thickness.

The *I–V* dependence of the area switched device is calculated using the current transport model and the material parameters listed in Table 1, with the oxygen vacancy concentration in the TiO_x depletion region being the only completely free parameter for the fit. The fits in Figure 6b show promising results as they qualitatively predict the curvature and trajectory of the *I–V* branches correctly. This clearly shows that the oxygen vacancy concentration in the TiO_x layer serves as a state variable for the area-type switching in $Pt/Al_2O_3/TiO_x/Cr/Pt$ devices. The $[V_O]$ values in the TiO_x layer used to match the different resistance states are $1.45\cdot10^{25}$, $1.65\cdot10^{25}$, $2.1\cdot10^{25}$, and $2.8\cdot10^{25}\ \text{m}^{-3}$. This result indicates that a change of $[V_O]$ by about a factor of two in the depletion region of TiO_x near the Al_2O_3 tunnel barrier is sufficient to change the average resistance value of the device by a factor of >50. Baeumer et al. reported the effect of redox-induced Schottky barrier variation for filamentary switching with the same polarity in graphene/$SrTiO_3$/Nb:$SrTiO_3$ devices. With a thickness of the undoped $SrTiO_3$ film of 20 nm, the authors found a filament diameter of ≈500 nm and donor concentrations in the near-interface region of $\approx 3 \times 10^{26}$–$8 \times 10^{26}\ \text{m}^{-3}$.[49] The observation of resistive switching at donor concentrations which are by almost a factor of 30 lower compared to the multifilamentary system might stem from the area-dependent nature of the resistive switching for the devices in this study. This is consistent with the clear area dependency, the absence of any detectable microstructural features, and with the proposed current transport model.

To investigate the current path at different voltages, the conduction band as a function of the z-position (blue lines) and the spectral current density as a function of the energy are plotted together in Figure 6c–h for two states with oxygen vacancies concentrations of $1.65\cdot10^{25}\ \text{m}^{-3}$ (c) to e), grey lines) and $2.8\cdot10^{25}\ \text{m}^{-3}$ (f) to h), red lines) and three voltages of 0.5 V, 1.5 V and 2.5 V (from bottom to top) each. The spectral current describes the fraction of current at each energy. The graphs in Figure 6e,h show that a tunneling process through the depletion zone in the TiO_x is the dominant transport mechanism at low to medium voltages for both values of $[V_O]$. This is also the region of read voltage for these devices. At increased voltages, the tunneling level shifts to higher energies until the Al_2O_3 band offset is reached (see Figure 6d,g,c,f). As a result, at high voltages, tunneling occurs through the Al_2O_3 for all concentrations. In summary, the resistance changes in the $Pt/Al_2O_3/TiO_x/Cr/Pt$ devices switched in area mode are caused by a broadening and enlargement of the depletion zone in the TiO_x near the Al_2O_3 tunneling barrier. The latter limits the maximum total current at high applied voltages. Comparable results based on the idea that a change in local donor concentration represented by oxygen vacancies bends the band structure and affects the resistance have been reported for

© 2023 The Authors. Advanced Electronic Materials published by Wiley-VCH GmbH

2199160x, 2023, 12, Downloaded from https://onlinelibrary.wiley.com/doi/10.1002/aelm.202300520, Wiley Online Library on [11/12/2023]. See the Terms and Conditions (https://onlinelibrary.wiley.com/terms-and-conditions) on Wiley Online Library for rules of use; OA articles are governed by the applicable Creative Commons License

2199160x, 2023, 12, Downloaded from https://onlinelibrary.wiley.com/doi/10.1002/aelm.202300520, Wiley Online Library on [11/12/2023]. See the Terms and Conditions (https://onlinelibrary.wiley.com/terms-and-conditions) on Wiley Online Library for rules of use; OA articles are governed by the applicable Creative Commons License

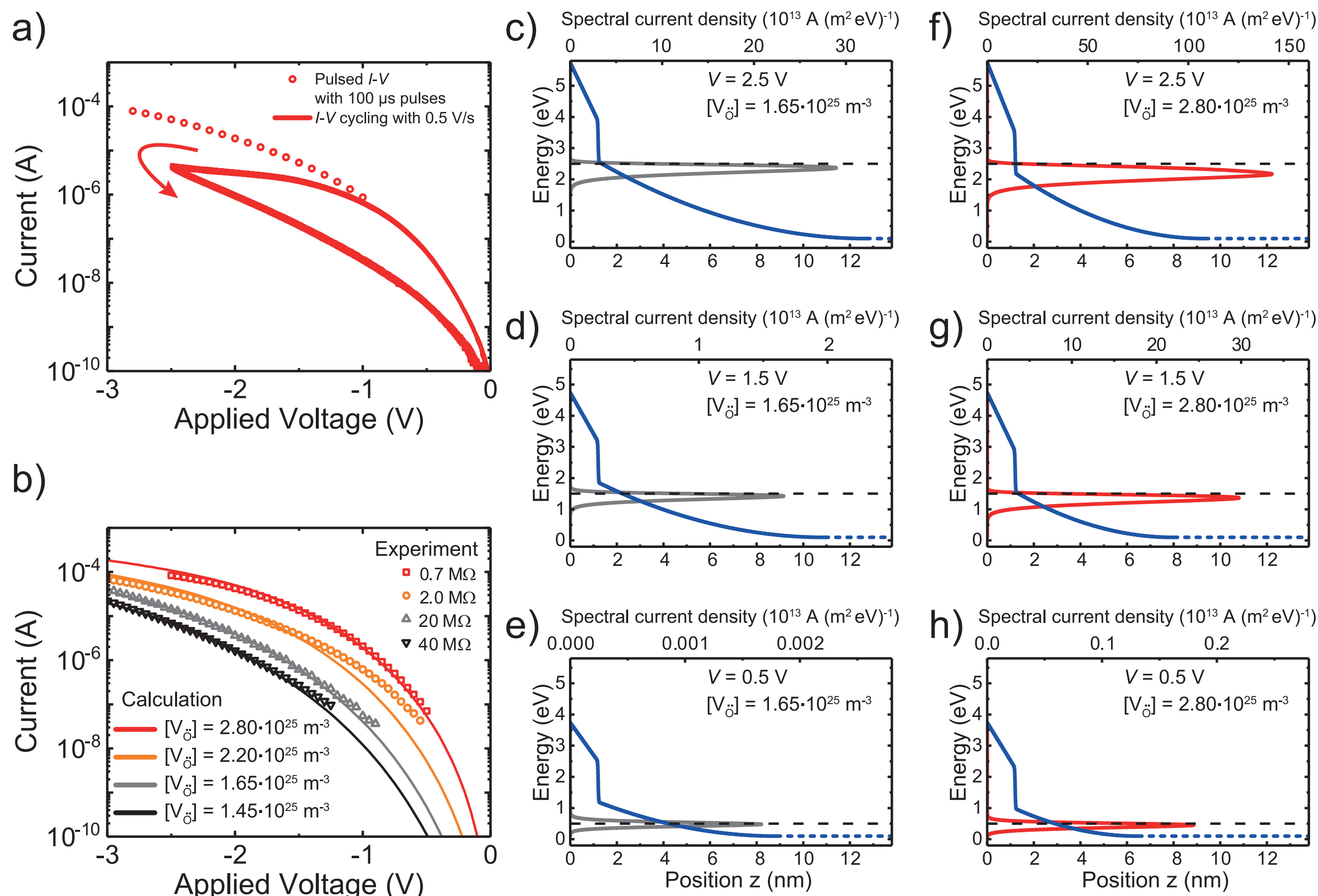

Figure 6. a) *I–V* curve of negative polarity for a (500 nm)^2 device switched in the area mode (red line) and an extended *I–V* characteristic (circles). b) Extended *I–V* measurements for negative polarity given by the symbols for two *a*-LRS (700 kΩ and 2 MΩ) and two *a*-HRS (20 and 40 MΩ) fitted by different concentrations of oxygen vacancies (colored lines). c–h) Conduction band energy versus position (blue lines) and spectral current density versus energy for two states with oxygen vacancies concentrations of $1.65\cdot10^{25}$ m^{-3} (grey lines) and $2.8\cdot10^{25}$ m^{-3} (red lines) and three voltages of 0.5, 1.5, and 2.5 V with the dashed black line indicating the quasi-Fermi-level in the Pt electrode.

different bilayer VCM devices made from a tunnel oxide and a n-type conducting oxide, such as TiO_{2-x}, $SrTiO_{3-x}$, and NbO_x.[17,23–24,63,76] In addition, Sommer et al.[77] investigated the effects of oxygen exchange between the two layers for a bilayer VCM cell consisting of a tunnel barrier and a highly doped conductive semiconductor employing a drift and diffusion model for electrons and oxygen vacancies. Oxygen exchange between the oxide layers was found for a low ion migration barrier in the tunnel oxide. This is consistent with the behavior of the $Pt/Al_2O_3/TiO_x/Cr/Pt$ devices in this study, where the calculations predict a change in $[V_O]$ between *a*-HRS and *a*-LRS less than $1.35\cdot10^{25}$ m^{-3}. At this small value of donor concentration, screening in the Al_2O_3 tunnel oxide does not occur. Thus, the tunnel barrier remains constant, as shown in Figure 6, and band bending takes place in the semiconducting TiO_x layer, resulting in the observed polarity of the switching hysteresis.

2.4. Discussion

Two switching modes have been identified in the same $Pt/Al_2O_3/TiO_x/Cr/Pt$ bilayer device consisting of amorphous films deposited by ALD, namely, a thin Al_2O_3 tunnel oxide and a semiconducting TiO_x layer. The modes differ by their area dependence of the resistance values in HRS and LRS, by the characteristics of the SET event, and by the polarity of the switching hysteresis. Devices that have not been subjected to an electroforming step exhibit gradual switching behavior for SET and RESET with a distinct area scaling of the resistance values in *a*-HRS and *a*-LRS. The SET event is triggered by a positive voltage applied to the Pt electrode. In contrast, devices that have subsequently undergone an electroforming step exhibit typical filamentary VCM-type resistive switching behavior with a more abrupt SET event occurring at negative voltage applied to the Pt Schottky electrode. The investigated material stack is ideally suited for fundamental studies on these two intensively discussed switching modes for several reasons: first, the two modes can be clearly distinguished by the application or non-application of an electroforming step; second, the memristive cells show reasonable switching stability in both modes; and third, the Ti L_{23} edge is readily accessible for spectroscopic studies. Here, the structural and chemical processes involved in the two switching processes have been investigated using operando spectromicroscopic techniques. The study is complemented by the analysis of the SET kinetic behavior of

 © 2023 The Authors. Advanced Electronic Materials published by Wiley-VCH GmbH

2199160x, 2023, 12, Downloaded from https://onlinelibrary.wiley.com/doi/10.1002/aelm.202300520, Wiley Online Library on [11/12/2023]. See the Terms and Conditions (https://onlinelibrary.wiley.com/terms-and-conditions) on Wiley Online Library for rules of use; OA articles are governed by the applicable Creative Commons License

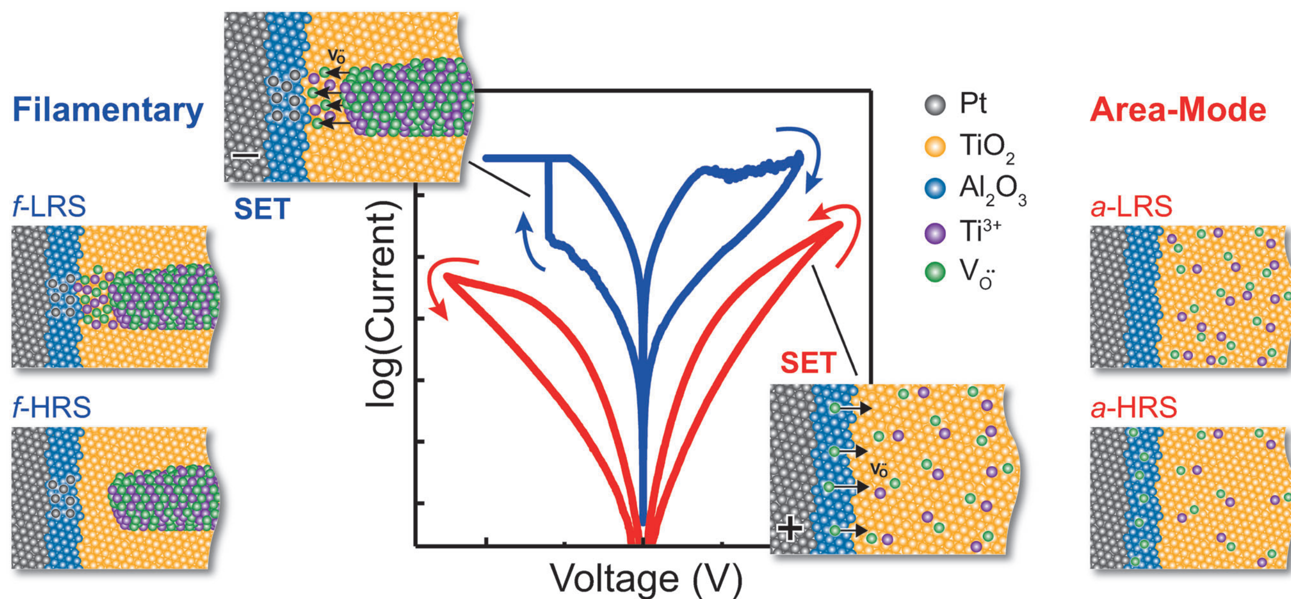

Figure 7. Comparison of the switching mechanism in standard filamentary mode with an abrupt SET event occurring for a negative voltage signal applied to the Pt active electrode and area-dependent switching with opposite polarity and quasi-analog behavior.

the different switching processes and the electronic conduction mechanism of the area switching devices.

For the device of 2 μm × 2 μm size switched in the filamentary mode, analysis of the NEXAFS spectra collected at the Ti L_{23} edge allowed identification of a filament of reduced TiO_{2-x} phase with a diameter of ≈50 nm, which is centrosymmetric surrounded by crystalline rutile-type TiO_2. This finding is supported by EELS data combined with the principal component analysis method. The temperature gradient from the filament to the surroundings can be estimated from the spatial extent of the rutile phase with a diameter of ≈1 μm, which results from local heating the 7 nm thin amorphous TiO_x layer to temperature of at least 670 K required for crystallization. This proves that Joule heating is a prerequisite for filamentary switching in these Al_2O_3/TiO_x layer stacks. These results are in good agreement with the standard filamentary VCM-type switching behavior described by a temperature-accelerated drift and diffusion of oxygen vacancies in the filament disk region. The switching properties as well as the measured SET kinetics are properly described by the physical JART v1b model.[78]

In contrast, TXM/NEXAFS analysis of the area switched device showed only signatures of amorphous titanium dioxide with no evidence of local structural or phase changes and with no significant changes in Ti L-edge absorption spectra for the devices set to either *a*-LRS or *a*-HRS. Therefore, extended *I*–*V* curves of a device in different *a*-HRS and *a*-LRS states were analyzed in terms of their electronic conduction mechanism. Due to the full area scaling, the numerical calculation could be simplified to a one-dimensional geometry. The $Pt/Al_2O_3/TiO_x/Cr$ cell is considered as a MOS capacitor in the depletion mode. The numerical calculations of the electronic current are performed with the oxygen vacancy concentration in the TiO_x layer serving as the state variable. Good agreement between the calculations and the extended *I*–*V* measurements is obtained for values of $[V_O]$ between $1.45 \cdot 10^{25}$ and $2.8 \cdot 10^{25}$ m^{-3} for the studied *a*-HRS and *a*-LRS, respectively. This shows that a change in donor concentration by $\approx 1.35 \cdot 10^{25}$ m^{-3}, changes the resistivity values at read voltage by a factor of ≈50, which is due to a change in band bending of the TiO_x layer near the Al_2O_3 interface. Given the low oxygen vacancy concentration on the order of 10^{25} m^{-3} and the small change by a factor of two due to switching, the operando spectroscopy analysis on the area switching devices could not reveal any change in the measured TXM spectra upon switching due to the resolution limits. The results described are consistently summarized in the schematics shown in **Figure 7**. Area mode switching (red hysteresis) can be realized in memristive bilayer devices, where one oxide serves as a tunneling barrier and the other oxide as highly n-doped conducting semiconductor. Switching is accomplished by broadening and enlarging the depletion zone of the semiconductor layer (TiO_x) near the tunnel barrier (Al_2O_3). The low oxygen vacancy concentration on the order of only 10^{25} m^{-3} is consistent with screening happening exclusively in the TiO_x layer, preserving the polarity of the area mode. Area scaling allows the resistor values to be matched to the desired circuit properties by device scaling.

The slower SET kinetics of the area-mode compared to the filamentary switching is attributed to the absence of Joule heating. This is confirmed by the results from spectromicroscopic analysis and the observation of a retained amorphous TiO_x phase. The resistance ratio achieved for quasi-analog switching in the $Pt/Al_2O_3/TiO_x/Cr/Pt$ devices is limited by the maximum RESET voltage that can be applied for the area mode prior to the onset of an electroforming event. Therefore, electroforming can be considered as a failure mechanism for the area-dependent switching. Due to the stochastic nature of electroforming events, the required voltage increases with decreasing defect density, increasing film thickness, and decreasing device area (see also Figure 1a).[79,80] Therefore, it is proposed that bilayer VCM-type

 © 2023 The Authors. Advanced Electronic Materials published by Wiley-VCH GmbH

devices of smaller dimensions are better suited for stable quasi-analog resistive switching in area mode. Since the Debye screening length is a function of film thickness, relative permittivity, and defect density, these parameters essentially define the design space of devices with gradual area switching.[77] For the $Pt/Al_2O_3/TiO_x/Cr/Pt$ devices investigated in this study, negligible band bending of the Al_2O_3 tunnel barrier is due to a quite small concentration of exchanged oxygen vacancies on the order of 10^{25} m^{-3}. Calculation of the spectral current density using the Tsu-Esaki-formalism revealed that the resistance ratio of *a*-HRS to *a*-LRS can be influenced by the choice of the optimal read voltage. An electroforming event results in filamentary switching (blue hysteresis in Figure 7). The influence of Joule heating for filamentary switching became obvious from the morphological changes observed in the surrounding of the filament. Based on the comprehensive characterization of the devices, the difference in SET kinetics between filamentary and area switching (c.f. Figure 1c)) can be clearly attributed to the influence of the locally generated heat in the filament, especially since identical cells were used. Changing the Al_2O_3 tunnel oxide from ≈1.2 to 2 nm thickness causes an increase in the SET time which is attributed to an increased voltage drop across the thicker tunnel barrier. This raises the question by which effective voltage the oxygen vacancy exchange at the oxide-oxide interface is accurately described.

3. Conclusion

In this study, the filamentary and area switching mode in Al_2O_3/TiO_x-based devices are directly compared utilizing the same physical cells at various sizes. Abrupt and gradual switching are correlated with the filamentary and area mode, respectively. For filamentary switching a localized region like Ti_4O_7 with ≈50 nm in diameter surrounded by crystalline rutile-like TiO_2 is identified, which confirms the effect of Joule heating in standard filamentary VCM-type devices with a fast SET kinetics. In contrast, TXM results of cells switched in area-mode showed that the TiO_x film was preserved in its amorphous phase, confirming that the local temperature did not exceed the crystallization temperature of ≈670 K. A negligible effect of Joule heating comes with a slower SET kinetics. Analysis of the electronic conduction mechanism of area-dependent states proposes a modulation of the effective tunnel barrier width due to oxygen ion reconfiguration at or a transfer across the Al_2O_3/TiO_x interface. A prerequisite for stable switching and self-limitation of the maximum current is a tunnel barrier with high dielectric strength and a negligible change of the band structure due to exchange of oxygen vacancies. These observations define the requirements for the design of quasi-analog type memristive devices based on area dependent VCM switching. In addition, the quasi-analog switching VCM devices are promising for energy-efficient neuromorphic computing applications due to their area-scalable resistance values with low variability.

4. Experimental Section

Fabrication of Micro- and Nano-Cross Point Devices: The crossbar devices consist of Ta (5 nm) / Pt (25 nm) / Al_2O_3 (1 – 2 nm) / TiO_x (7 nm) / Cr (5 nm) / Pt (15 nm) structures with sizes of $4\cdot10^{-3}$–9 μm² grown on SiO_2/Si substrates. The 25 nm thick Pt bottom electrode (BE) was obtained from sputter deposition, patterning by e-beam lithography for nanostructures and optical lithography for microstructures and structuring by reactive ion beam etching (RIBE). Subsequently, ultrathin metal oxide layers were grown by atomic layer deposition (ALD) in a FlexAL ALD Tool of Oxford Plasma Technologies. Al_2O_3 layers of 1.2, 1.5, and 2 nm, and a TiO_x layer of 7 nm thickness were obtained from trimethyl aluminum (TMA) and O_2-plasma, and tetrakis(dimethyl-amino) titanium (TDMAT) and H_2O vapor, respectively. The growth rates in the unit of growth per cycle for the TiO_x and Al_2O_3 films deposited at 250 °C were ≈0.035 and 0.1 nm/cycle, respectively. The thickness of the individual layers grown in this study was controlled by X-ray reflectivity measurements on a Bruker D8 Discover A25 diffractometer equipped with a Cu K_α source and operated at 40 kV and 40 mA. The metal layers for the top electrode (TE) composed of Cr and Pt as a capping layer were obtained from sputtering. The TE lines together with the underlying switching oxide were structured in a RIBE process. Cr was used rather than the more strongly reducing Ti to avoid any background Ti signal in the subsequent spectromicroscopic measurements and to have similar devices for the micro- and nanostructures compared to the membrane structures.

Micro-Crosspoint Devices on Si_3N_4 Membranes: For near edge X-ray absorption fine structure (NEXAFS)-TXM measurements the total sample thickness is reduced to under 100 nm to achieve a good signal-to-noise ratio. For this purpose, the stack itself is adjusted to Ta (3 nm) / Pt (15 nm) / Al_2O_3 (1.5 nm) / TiO_x (7 nm) / Cr (5 nm) / Pt (15 nm) and the crossbars were fabricated on 40 nm Si_3N_4/Si. By etching windows into the silicon substrate from the backside until the Si_3N_4 is reached, the device structure was only supported by the free-standing Si_3N_4 membrane so that the total sample thickness that is transmitted by the X-rays is ≈85 nm.

Device Measurement and Characterization: Electrical characterization comprised sweep and fast pulse analysis. First was carried out by an Agilent B1500A semiconductor analyzer with a sweep rate of 1 V s^{-1}. Second was mainly performed identically to ref. [16] on a Keithley 4200 SCS, equipped with a two-channel pulse measure unit (4225-PMU) and two remote amplifiers (4225-RPM), and expanded by measurements on a Keithley 2611 for the area mode. Voltage polarity is always defined toward the Pt bottom electrode, as the electronically active electrode. For the area mode the fast pulse analysis was carried out after an initialization with 200 pulses of alternating voltage of ± 2.0 V and 1 s pulse time each. The resistances before and after the potential SET pulse were calculated from the current values obtained at −0.5 V. If the ratio of the resistance value before and after SET was >5, this was defined as a switching event. To establish compatibility of the measurements, prior to the application of a SET pulse, the cell was transformed into a defined HRS of 200 MΩ ± 10%. RESET pulses of 1 s length and increasing height were applied if the cell's resistance was below this value.

Transmission X-ray Microscopy: NEXAFS-TXM measurements were performed at the undulator beamline U41-PGM1 at the BESSY II electron storage ring operated by the Helmholtz-Zentrum Berlin.[81] At this endstation, Ti L-edge spectra can be measured with a spectral resolution of up to $E/\Delta E = 10^4$ and a spatial resolution of 25 nm.[82] With NEXAFS the switching layer can be investigated isolated from the electrodes by tuning the photon energy to the Ti resonance, here the Ti $L_{2,3}$ absorption edge (455–470 eV). The absorption intensity is proportional to the unoccupied density of states providing information about the crystal structure and oxidation state of the TiO_x layer.[83] The signal-to-noise ratio for the O K-edge has been too weak and the signal of Cr L-edge has been dominated by components in the system so that these could not be used for meaningful conclusions. The X-ray absorption spectra at the Ti L-edge were extracted from image sequences acquired in the photon energy range 452–470 eV. Three separate images were acquired at each photon energy and summed up to improve the signal to noise ratio. Each image was taken with proper focus on the sample to optimize the spatial resolution. The image series were then aligned using a cross-correlation iteration process to get rid of the sample movement. The spectra are normalized by nearby reference signal without Ti-signature to take inhomogeneity of the beam intensity in account.

© 2023 The Authors. Advanced Electronic Materials published by Wiley-VCH GmbH

2199160x, 2023, 12, Downloaded from https://onlinelibrary.wiley.com/doi/10.1002/aelm.202300520, Wiley Online Library on [11/12/2023]. See the Terms and Conditions (https://onlinelibrary.wiley.com/terms-and-conditions) on Wiley Online Library for rules of use; OA articles are governed by the applicable Creative Commons License

Transmission Electron Microscopy: HAADF-STEM imaging and STEM-EELS measurements were performed with a spherical aberration-corrected TEM (Titan G2 80–200 ChemiSTEM, FEI) at an operating voltage of 200 kV equipped with a Cs probe corrector, a Schottky type high-brightness X-FEG module, and a post-column energy filter system (Enfinium ER 977, Gatan). The spectra were recorded by spectral mapping in the energy range between 400 and 600 eV to include Ti *L*- and Cr *L*-edges.

Supporting Information

Supporting Information is available from the Wiley Online Library or from the author.

Acknowledgements

This work was in part funded by the German Research Foundation (DFG) under Grant No. SFB 917, in part by the Federal Ministry of Education and Research (BMBF, Germany) in the projects NEUROTEC (Project Nos. 16ME0398K and 16ME0399) and NeuroSys (Project No. 03ZU1106AB) and is based on the Jülich Aachen Research Alliance (JARA-FIT). Support of Grigory Potemkin and Clemens Wiedenhöft in sample fabrication and of Marcel Gerst for technical assistance is gratefully acknowledged. The authors thank the Helmholtz–Zentrum Berlin für Materialien und Energie for the allocation of synchrotron radiation beamtime.

Open access funding enabled and organized by Projekt DEAL.

Conflict of Interest

The authors declare no conflict of interest.

Data Availability Statement

The data that support the findings of this study are available from the corresponding author upon reasonable request.

Keywords

analog, digital, electron energy loss spectroscopy, electronic conduction mechanism, memristors, ReRAM, transmission X-ray microscopy

Received: August 2, 2023
Revised: September 8, 2023
Published online: October 5, 2023

[1] D. V. Christensen, R. Dittmann, B. Linares-Barranco, A. Sebastian, M. Le Gallo, A. Redaelli, S. Slesazeck, T. Mikolajick, S. Spiga, St. Menzel, I. Valov, G. Milano, C. Ricciardi, S.-J. Liang, F. Miao, M. Lanza, T. J. Quill, S. T. Keene, A. Salleo, J. Grollier, D. Markovic, A. Mizrahi, P. Yao, J. J. Yang, G. Indiveri, J. P. Strachan, S. Datta, E. Vianello, A. Valentian, J. Feldmann, et al., *Neuromorph. Comput. Eng.* **2022**, *2*, 022501.
[2] F. Kiani, J. Yin, Z. Wang, J. J. Yang, Q. Xia, *Sci. Adv.* **2021**, *7*, eabj4801.
[3] C. X. Xue, Y. C. Chiu, T. W. Liu, T. Y. Huang, J. S. Liu, T. W. Chang, H. Y. Kao, J. H. Wang, S. Y. Wei, C. Y. Lee, S. P. Huang, J. M. Hung, S. H. Teng, W. C. Wei, Y. R. Chen, T. H. Hsu, Y. K. Chen, Y. C. Lo, T. H. Wen, C. C. Lo, R. S. Liu, C. C. Hsieh, K. T. Tang, M. S. Ho, C. Y. Su, C. C. Chou, Y. D. Chih, M. F. Chang, *Nat. Electron.* **2021**, *4*, 81.
[4] R. Dittmann, S. Menzel, R. Waser, *Adv. Phys.* **2021**, *70*, 155.
[5] D.-H. Kwon, K. M. Kim, J. H. Jang, J. M. Jeon, M. H. Lee, G. H. Kim, X.-S. Li, G.-S. Park, B. Lee, S. Han, M. Kim, C. S. Hwang, *Nat. Nanotechnol.* **2010**, *5*, 148.
[6] J. P. Strachan, M. D. Pickett, J. J. Yang, S. Aloni, A. L. David Kilcoyne, G. Medeiros-Ribeiro, R. Stanley Williams, *Adv. Mater.* **2010**, *22*, 3573.
[7] J. P. Strachan, M. D. Pickett, J. J. Yang, S. Aloni, A. L. David Kilcoyne, G. Medeiros-Ribeiro, R. S. Williams, *Adv. Mater.* **2010**, *22*, 3573.
[8] D. Carta, A. P. Hitchcock, P. Guttmann, A. Regoutz, A. Khiat, A. Serb, I. Gupta, T. Prodromakis, *Sci. Rep.* **2016**, *6*, 21525.
[9] D. Carta, I. Salaoru, A. Khiat, A. Regoutz, C. Mitterbauer, N. M. Harrison, T. Prodromakis, *ACS Appl. Mater. Interfaces* **2016**, *8*, 19605.
[10] S. Menzel, R. Waser, in *Advanced in Non-Volatile Memory and Storage Technology*, 2nd ed. (Eds: B. Magyari-Köpe, Y. Nishi), Woodhead Publishing, Sawston, Cambridge **2019**, Ch. 4, 137.
[11] J. Zhu, T. Zhang, Y. Yang, R. Huang, *Appl. Phys. Rev.* **2020**, *7*, 011312.
[12] A. Sawa, T. Fujii, M. Kawasaki, Y. Tokura, *Appl Phys Lett* **2004**, *85*, 4073.
[13] Y. Kim, Y. J. Kwon, D. E. Kwon, K. J. Yoon, J. H. Yoon, S. Yoo, H. J. Kim, T. H. Park, J.-W. Han, K. M. Kim, C. S. Hwang, *Adv. Mater.* **2018**, *30*, 1704230.
[14] A. Herpers, C. Lenser, C. Park, F. Offi, F. Borgatti, G. Panaccione, S. Menzel, R. Waser, R. Dittmann, *Adv. Mater.* **2014**, *26*, 2730.
[15] K. M. Kim, J. Zhang, C. Graves, J. J. Yang, B. J. Choi, C. S. Hwang, Z. Li, R. S. Williams, *Nano Lett.* **2016**, *16*, 6724.
[16] B. Arndt, F. Borgatti, F. Offi, M. Phillips, P. Parreira, T. Meiners, S. Menzel, K. Skaja, G. Panaccione, D. A. MacLaren, R. Waser, R. Dittmann, *Adv. Funct. Mater.* **2017**, *27*, 1702282.
[17] S. Siegel, C. Baeumer, A. Gutsche, M. von Witzleben, R. :. Waser, S. Menzel, R. Dittmann, *Adv. Electron. Mater.* **2021**, *7*, 2000815.
[18] A. Gutsche, S. Siegel, J. Zhang, S. Hambsch, R. Dittmann, *Front Neurosci* **2021**, *15*, 661261.
[19] R. Wang, T. Shi, X. Zhang, W. Wang, J. Wei, J. Lu, X. Zhao, Z. Wu, R. Cao, S. Long, Q. Liu, M. Liu, *Materials* **2018**, *11*, 2102.
[20] M. Kim, M. A. Rehman, D. Lee, Y. Wang, D. Lim, M. F. Khan, H. Choi, Q. Y. Shao, J. Suh, H. Lee, H. Park, *ACS Appl. Mater. Interfaces* **2022**, *14*, 44561.
[21] D. S. Kuzmichev, A. G. Chernikova, M. G. Kozodaev, A. M. Markeev, *Phys. Status Solidi A* **2020**, *217*, 1900952.
[22] T. Stecconi, R. Guido, L. Berchialla, A. La Porta, J. Weiss, Y. Popoff, M. Halter, M. Sousa, F. Horst, D. Davila, U. Drechsler, R. Dittmann, B. J. Offrein, V. Bragaglia, *Adv. Electron. Mater.* **2022**, *8*, 2200448.
[23] S. Dirkmann, M. Hansen, M. Ziegler, H. Kohlstedt, T. Mussenbrock, *Sci. Rep.* **2016**, *6*, 35606.
[24] S. Yarragolla, T. Hemke, J. Trieschmann, F. Zahari, H. Kohlstedt, T. Mussenbrock, *J. Appl. Phys.* **2022**, *131*, 134304.
[25] T. L. Tsai, Y. H. Lin, T. Y. Tseng, *IEEE Electron Device Lett.* **2015**, *36*, 675.
[26] Q. Luo, X. Zhang, Y. Hu, T. Gong, X. Xu, P. Yuan, H. Ma, D. Dong, H. Lv, S. Long, Q. Liu, M. Liu, *IEEE Electron Device Lett.* **2018**, *39*, 664.
[27] S. Park, B. Spetzler, T. Ivanov, M. Ziegler, *Sci. Rep.* **2022**, *12*, 18266.
[28] M. Hellenbrand, B. Bakhit, H. Dou, M. Xiao, M. O. Hill, Z. Sun, A. Mehonic, A. Chen, Q. Jia, H. Wang, J. L. MacManus-Driscoll, *Sci. Adv.* **2023**, *9*, eadg1946.
[29] B. Govoreanu, L. D. Piazza, J. Ma, T. Conard, A. Vanleenhove, A. Belmonte, D. Radisic, M. Popovici, A. Velea, A. Redolfi, O. Richard, S. Clima, C. Adelmann, H. Bender, M. Jurczak, 2016 IEEE Symp. on VLSI Technology, Honolulu, HI, USA, June **2016**.
[30] S. Stathopoulos, A. Khiat, M. T.: S. Cortese, A. Serb, I. Valov, T. Prodromakis, *Sci. Rep.* **2017**, *7*, 17532.
[31] S. Aussen, F. Cüppers, R. Waser, S. Hoffmann-Eifert, *2022 IEEE 22nd Int. Conf. on Nanotechnology (NANO)*, Palma de Mallorca, Spain, July **2022**.
[32] C. Funck, S. Menzel, *ACS Appl. Electron. Mater.* **2021**, *3*, 3674.
[33] K. Schnieders, C. Funck, F. Cüppers, S. Aussen, T. Kempen, A. Sarantopoulos, R. Dittmann, S. Menzel, V. Rana, S. Hoffmann-Eifert, S. Wiefels, *APL Mater.* **2022**, *10*, 101114.
[34] R. Dittmann, S. Menzel, R. Waser, *Adv. Phys.* **2022**, *70*, 155.
[35] S. Fusi, L. F. Abbott, *Nat. Neurosci.* **2007**, *10*, 485.

© 2023 The Authors. Advanced Electronic Materials published by Wiley-VCH GmbH

2199160x, 2023, 12, Downloaded from https://onlinelibrary.wiley.com/doi/10.1002/aelm.202300520, Wiley Online Library on [11/12/2023]. See the Terms and Conditions (https://onlinelibrary.wiley.com/terms-and-conditions) on Wiley Online Library for rules of use; OA articles are governed by the applicable Creative Commons License

[36] E. Covi, S. Brivio, A. Serb, T. Prodromakis, M. Fanciulli, S. Spiga, *Front Neurosci* **2016**, *10*, 6.
[37] J. Frascaroli, S. Brivio, E. Covi, S. Spiga, *Sci. Rep.* **2018**, *8*, 7178.
[38] T. Gokmen, W. Haensch, *Front Neurosci* **2020**, *14*, 103.
[39] C. Bengel, F. Cüppers, M. Payvand, R. Dittmann, R. Waser, S. Hoffmann-Eifert, S. Menzel, *Front Neurosci* **2021**, *15*, 621.
[40] F. Cüppers, S. Menzel, C. Bengel, A. Hardtdegen, M. von Witzleben, U. Böttger, R. Waser, S. Hoffmann-Eifert, *Appl. Phys. Lett.: Mater.* **2019**, *7*, 091105.
[41] A. Ascoli, S. Menzel, V. Rana, T. Kempen, I. Messaris, A. S. Demirkol, M. Schulten, A. Siemon, R. Tetzlaff, *Adv. Electron. Mater.* **2022**, *8*, 2200182.
[42] S. Menzel, M. Waters, A. Marchewka, U. Böttger, R. Dittmann, R. Waser, *Adv. Funct. Mater.* **2011**, *21*, 4487.
[43] D. Cooper, C. Baeumer, N. Bernier, A. Marchewka, C. La Torre, R. E. Dunin-Borkowski, S. Menzel, R. Waser, R. Dittmann, *Adv. Mater.* **2017**, *29*, 1700212.
[44] T. Heisig, C. Baeumer, U. N. Gries, M. P. Mueller, C. La Torre, M. Luebben, N. Raab, H. Du, S. Menzel, D. N. Mueller, C.-L. Jia, J. Mayer, R. Waser, I. Valov, R. A. De Souza, R. Dittmann, *Adv. Mater.* **2018**, *30*, 1800957.
[45] A. F. Zurhelle, W. Stehling, R. Waser, R. A. De Souza, S. Menzel, *Adv. Mater. Interfaces* **2022**, *9*, 2101257.
[46] K. Fleck, C. La Torre, N. Aslam, S. Hoffmann-Eifert, U. Böttger, S. Menzel, *Phys. Rev. Appl.* **2016**, *6*, 064015.
[47] H. Du, C. Jia, A. Koehl, J. Barthel, R. Dittmann, R. Waser, J. Mayer, *Chem. Mater.* **2017**, *29*, 3164.
[48] J. P. Strachan, G. Medeiros-Ribeiro, J. J. Yang, M.-X. Zhang, F. Miao, I. Goldfarb, M. Holt, V. Rose, R. S. Williams, *Appl. Phys. Lett.* **2011**, *98*, 242114.
[49] C. Baeumer, C. Schmitz, A. Marchewka, D. N. Mueller, R. Valenta, J. Hackl, N. Raab, S. P. Rogers, M. I. Khan, S. Nemsak, M. Shim, S. Menzel, C. M. Schneider, R. Waser, R. Dittmann, *Nat. Commun.* **2016**, *7*, 12398.
[50] A. Koehl, H. Wasmund, A. Herpers, P. Guttmann, S. Werner, K. Henzler, H. Du, J. Mayer, R. Waser, R. Dittmann, *APL Mater.* **2013**, *1*, 042102.
[51] C. Baeumer, R. Valenta, C. Schmitz, A. Locatelli, T. O. Mentes, S. P. Rogers, A. Sala, N. Raab, S. Nemsak, M. Shim, C. M. Schneider, S. Menzel, R. Waser, R. Dittmann, *ACS Nano* **2017**, *11*, 6921.
[52] F. M. F. de Groot, M. O. Figueiredo, M. J. Basto, M. Abbate, H. Petersen, J. C. Fuggle, *Phys. Chem. Miner.* **1992**, *19*, 140.
[53] E. Stoyanov, F. Langenhorst, G. Steinle-Neumann, *Am. Mineral.* **2007**, *92*, 577.
[54] M. Abbate, F. M. F. de Groot, J. C. Fuggle, A. Fujimori, Y. Tokura, Y. Fujishima, O. Strebel, M. Domke, G. Kaindl, J. van Elp, B. T. Thole, G. A. Sawatzky, M. Sacchi, N. Tsuda, *Phys Rev B Condens Matter* **1991**, *44*, 5419.
[55] A. C. Dippel, O. Gutowski, L. Klemeyer, U. Boettger, F. Berg, T. Schneller, A. Hardtdegen, S. Aussen, S. Hoffmann-Eifert, M. V. Zimmermann, *Nanoscale* **2020**, *12*, 13103.
[56] M. Fusi, E. Maccallini, T. Caruso, C. S. Casari, A. L. Bassi, C. E. Bottani, P. Rudolf, K. C. Prince, R. G. Agostino, *Surf. Sci.* **2011**, *605*, 333.
[57] S. O. Kucheyev, T. F. Baumann, Y. M. Wang, T. v. Buuren, J. F. Poco, J. J. H. Satcher, A. V. Hamza, *Appl. Phys. Lett.* **2006**, *88*, 103117.
[58] M. Lopez, L. Soriano, F. Palomares, M. Sanchez-Agudo, G. Fuentes, A. Gutierrez, J. Jimenez, *Surf. Interface Anal.* **2002**, *33*, 570.
[59] A. Ohtomo, D. A. Muller, J. L. Grazul, H. Y. Hwang, *Appl. Phys. Lett.* **2002**, *80*, 3922.
[60] L. Soriano, M. Abbate, J. Vogel, J. C. Fuggle, A. Fernández, A. R. González-Elipe, M. Sacchi, J. M. Sanz, *Surf. Sci.* **1993**, *290*, 427.
[61] J. Meng, J. M. Goodwill, E. Strelcov, K. Bao, J. J. McClelland, M. Skowronski, *ACS Appl. Electron. Mater.* **2023**, *5*, 2414.
[62] S. Seong, E. Lee, H. W. Kim, B. I. Min, S. Lee, J. Dho, Y. Kim, J.-Y. Kim, J.-S. Kang, *J. Magn. Magn. Mater.* **2018**, *452*, 447.
[63] H. Zhang, S. Yoo, S. Menzel, C. Funck, F. Cüppers, D. J. Wouters, C. S. Hwang, R. Waser, S. Hoffmann-Eifert, *ACS Appl. Mater. Interfaces* **2018**, *10*, 29766.
[64] C. Funck, C. Bäumer, S. Wiefels, T. Hennen, R. Waser, S. Hoffmann-Eifert, R. Dittmann, S. Menzel, *Phys Rev B Condens Matter* **2020**, *102*, 035307.
[65] H. Zhang, N. Aslam, M. Reiners, R. Waser, S. Hoffmann-Eifert, *Chem. Vap. Deposition* **2014**, *20*, 282.
[66] M. Reiners, K. Xu, N. Aslam, A. Devi, R. Waser, S. Hoffmann-Eifert, *Chem. Mater.* **2013**, *25*, 2934.
[67] S. M. Sze, K. K. Ng, *Physics of Semiconductor Devices*, John Wiley & Sons Inc., New York **2007**.
[68] R. Tsu, L. Esaki, *Appl. Phys. Lett.* **1973**, *22*, 562.
[69] G. Wentzel, *Z. Phys.* **1926**, *38*, 518.
[70] H. A. Kramers, *Z. Phys.* **1926**, *39*, 828.
[71] N. Rausch, E. P. Burte, *Microelectron. Eng.* **1992**, *19*, 725.
[72] J. Acharya, J. Wilt, B. Liu, J. Wu, *ACS Appl. Mater. Interfaces* **2018**, *10*, 3112.
[73] M. L. Huang, Y. C. Chang, C. H. Chang, T. D. Lin, J. Kwo, T. B. Wu, M. Hong, *Appl. Phys. Lett.* **2006**, *89*, 12903.
[74] F. Hossein-Babaei, M. M. Lajvardi, N. Alaei-Sheini, *Appl. Phys. Lett.* **2015**, *106*, 83503.
[75] K. Fleck, U. Böttger, R. Waser, S. Menzel, *IEEE Electron Device Lett.* **2014**, *35*, 924.
[76] C. Baeumer, T. Heisig, B. Arndt, K. Skaja, F. Borgatti, F. Offi, F. Motti, G. Panaccione, R. Waser, S. Menzel, R. Dittmann, *Faraday Discuss.* **2019**, *213*, 215.
[77] N. Sommer, R. Dittmann, S. Menzel, *Phys. Rev. Appl.* **2023**, *19*, 044084.
[78] C. Bengel, A. Siemon, F. Cüppers, S. Hoffmann-Eifert, A. Hardtdegen, M. von Witzleben, L. Hellmich, R. Waser, S. Menzel, *IEEE Trans Circuits Syst I Regul Pap* **2020**, *67*, 4618.
[79] B. Govoreanu, G. S. Kar, Y.-Y. Chen, V. Paraschiv, S. Kubicek, A. Fantini, I. P. Radu, L. Goux, S. Clima, R. Degraeve, N. Jossart, O. Richard, T. Vandeweyer, K. Seo, P. Hendrickx, G. Pourtois, H. Bender, L. Altimime, D. J. Wouters, J. A. Kittl, M. Jurczak, *IEDM Technical Digest*, Washington, DC, USA, December **2011**.
[80] A. Chen, *71st Device Research Conf.*, Notre Dame, IN, USA, June **2013**, 181–182.
[81] P. Guttmann, S. Werner, F. Siewert, A. Sokolov, J. Schmidt, M. Mast, M. Brzhezinskaya, C. Jung, R. Follath, G. Schneider, *Microsc. Microanal.* **2018**, *24*, 204.
[82] P. Guttmann, C. Bittencourt, S. Rehbein, P. Umek, X. Ke, G. Van Tendeloo, C. P. Ewels, G. Schneider, *Nat. Photonics* **2012**, *6*, 25.
[83] G. van der Laan, *Phys Rev B Condens Matter* **1990**, *41*, 12366.

© 2023 The Authors. Advanced Electronic Materials published by Wiley-VCH GmbH

2199160x, 2023, 12, Downloaded from https://onlinelibrary.wiley.com/doi/10.1002/aelm.202300520, Wiley Online Library on [11/12/2023]. See the Terms and Conditions (https://onlinelibrary.wiley.com/terms-and-conditions) on Wiley Online Library for rules of use; OA articles are governed by the applicable Creative Commons License